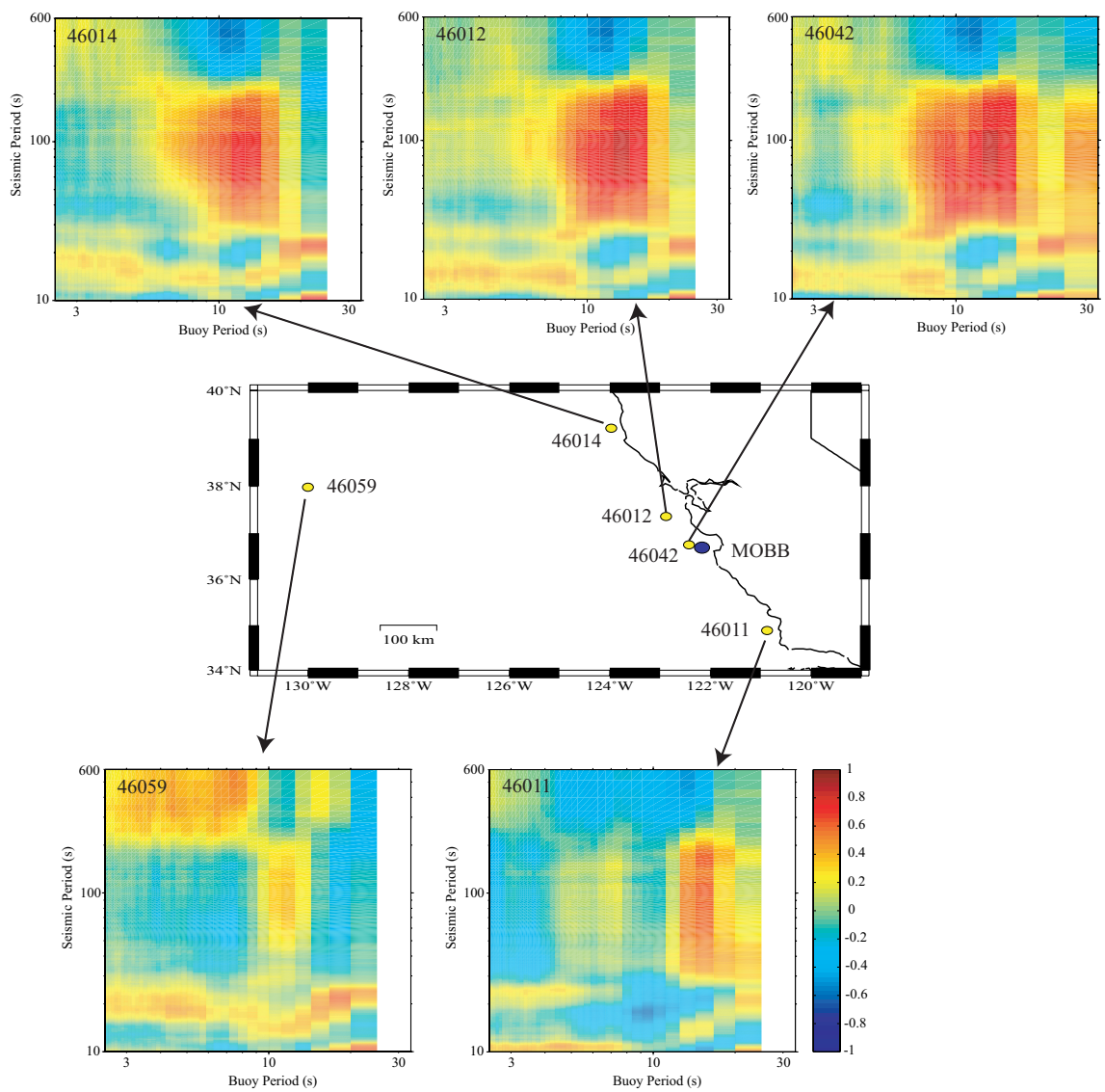
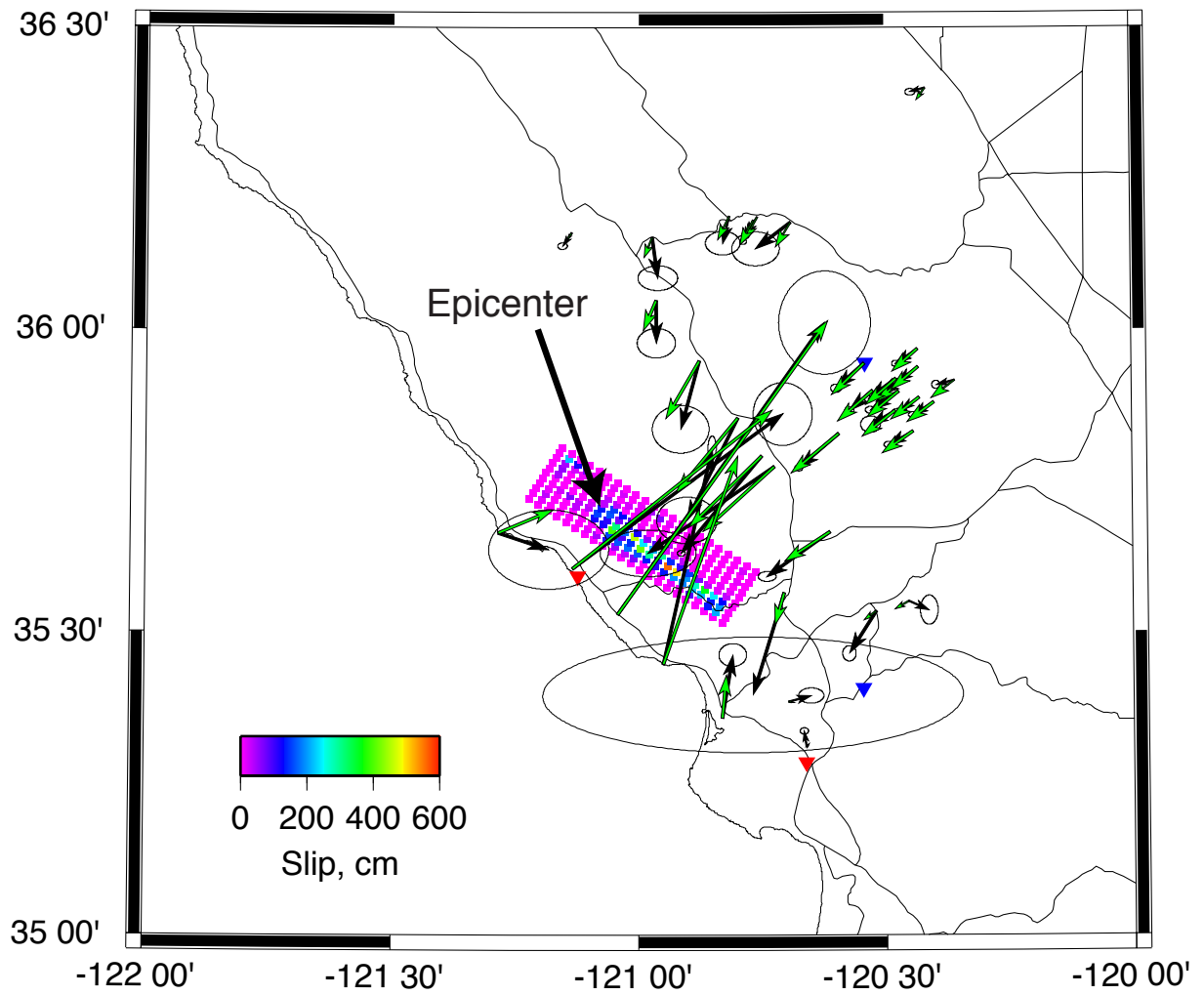


Chapter 12

Research Studies





1. Periodic Earthquake Rate Variations on the San Andreas Fault

Robert M. Nadeau

1.1 Slip Rates from Micro-quakes

A characteristically repeating micro-earthquake sequence (CS) is a sequence of small earthquakes ($M \sim < 3.5$) whose seismograms, locations and magnitudes are nearly identical. Each earthquake in the sequence represents a repeated rupture of the same patch of fault, and the times between the ruptures (i.e., their recurrence intervals) are, in general, inversely proportional to the average tectonic loading rate on the fault (*Nadeau and McEvilly, 1999; Bürgmann et al., 2000; Igarashi et al., 2003*). Their unique properties allow CS to be used to infer fault slip rates at depth on faults, and this capability has been proven to be particularly useful in regions where geodetic measurements are limited in spatial coverage and frequency.

1.2 Repeating Quake Analysis

Along much of the 175 km stretch of the San Andreas Fault (SAF) separating the rupture zones of California's two great earthquakes (i.e., the \sim M8 1906 San Francisco and 1857 Fort Tejon events), geodetic measurements have been done relatively infrequently in campaign mode. Along this stretch, however, over 500 CS have been identified with events occurring between 1984 and 1999 (inclusive). And, analysis of these sequences reveal: 1) that the recurrence intervals within any given CS vary significantly, 2) that among different CS on a given fault segment the recurrence variations are coherent through time and 3) that in many cases the coherent variations recurred quasi-periodically (*Nadeau and McEvilly, 2004*).

1.3 Correlation with Larger Earthquakes

Recurrence variation information was used to construct a profile of deep fault slip rate histories along the 175 km study zone for the 1984-1999 study period (*Nadeau and McEvilly, 2004*). The profile reveals that along the northwestern-most 80 km segment of the study zone (Figure 12.1), deep fault slip rates commonly vary by over 100% and their variation patterns (i.e., pulse patterns) recur with a periodicity of ~ 3 years. Shown at the right in Figure 12.1 is a comparison of this large-scale periodic deep slip pattern with the occurrence times of M3.5 to M7.1 earthquakes (i.e., magnitudes larger than those of the CS events) and with the occurrence times of three known slow slip events in the area (*Linde et al., 1996; Gwyther et al., 2000*). The comparison reveals a significant correlation between the onset periods of the repeating deep slip signals and the occurrence rates of

the larger events.

To the resolution of the characteristic microearthquake slip rate data, the M7.1 Loma Prieta mainshock occurred coincident with the onset of the P2 timed pulse (Figure 12.1, right). The times of the next two largest non-aftershock events in the area and study period (i.e., M5.4 San Juan Bautista mainshock in 1998 and a M4.7 event in 1986) are also coincident with the onset of pulses P5 and P1, respectively, and the P3, P4, and P5 pulse onsets correspond closely to the times of the three slow slip events in the area whose aseismic moment magnitudes were estimated to be $\sim 5M_w$ (*Linde et al., 1996; Gwyther et al., 2000*).

Excluding Loma Prieta aftershocks, 45 earthquakes with $M > 3.5$ occurred in region during the 1984-1999 study period, and a general correlation is also observed between the occurrence times of these events and the 1-year onset periods of the pulses (i.e. the time interval where pulse slip velocities transition from low to high values). Thirty-three of the 45 events were found to occur during the onset periods, this represents an occurrence rate that is 6 times larger than the rate observed during the non-onset periods. When Loma Prieta aftershocks are included into the analysis the onset period rate increased to 7 times that of the non-onset period rate (Figure 12.1, right).

1.4 Implications

Earthquake triggering induced by velocity weakening effects (*Dietrich, 1986; Scholz, 1990*) associated with increasing fault slip velocities may provide an explanation for the increased rates of the larger earthquakes during the pulse onsets. It is also possible that the increased rates occur quasi-periodically due to some other mechanism, such as the accelerated accumulation of failure during quasi-periodic tectonic loading.

Continued monitoring of the $M > 3.5$ earthquake activity occurring since the 1984-1999 analysis period along the 80 km SAF segment shows that the quasi-periodic occurrence rate pattern for larger quakes is continuing and that the timing of the rate increases remains consistent with the projected pulse onset times based on the 1984-1999 pulsing statistics (Figure 12.1, right-top). As a consequence analysis of the post-1999 CS seismicity has now been initiated in order to confirm the continuance of the deep slip rate pulsing that the larger magnitude seismicity patterns suggest may be taking place.

Regardless of the outcome of this subsequent analysis, however, the the ongoing quasi-periodic patterns of

the larger earthquake rates holds the potential for refinement of time-dependent earthquake forecasts models for this area (WGCEP, 1999; Matthews *et al.*, 2002) to time scales comparable to the average pulse cycle duration of ~ 3 years that is observed.

1.5 Acknowledgements

Thanks are given to Roland Bürgmann and Mark H. Murray for stimulating conversations and inciteful comments regarding this work. This research was supported by the U.S. Geological Survey through awards 02HQGR0067 and 03HQGR0065 and by the National Science Foundation through award 9814605.

1.6 References

Bürgmann, R., D. Schmidt, R.M. Nadeau, M. d'Alessio, E. Fielding, D. Manaker, T.V. McEvilly, and M.H. Murray, Earthquake Potential along the Northern Hayward Fault, California, *Science*, 289, 1178-1182, 2000.

Dieterich, J.H., A model for the nucleation of earthquake slip, in *Earthquake Source Mechanics*, S. Das, J. Boatwright, and C.H. Scholz (Editors), *American Geophysical Monograph 37*, American Geophysical Union, Washington, D.C., 37-47, 1986.

Gwyther, R.L., C.H. Thurber, M.T. Gladwin, and M. Mee, Seismic and Aseismic Observations of the 12th August 1998 San Juan Bautista, California, M5.3 Earthquake, in *Proceedings of the 3rd Conference on tectonic problems of the San Andreas Fault system*, G. Bokelmann and R. Kovach, Eds., *Stanford California School of Earth Sciences*, Stanford University, 2000.

Igarashi, T., T. Matsuzawa, and A. Hasegawa, Repeating earthquakes and interplate aseismic slip in the northeastern Japan subduction zone, *J. Geophys. Res.*, 108, 2249, doi:10.1029/2002JB001920, 2003.

Linde, A.T., M.T. Gladwin, M.J.S. Johnston, R.L. Gwyther, and R. Bilham, A slow earthquake near San Juan Bautista, California, in December, 1992, *Nature*, 383, 65-68, 1996.

Matthews, M.V., W.L. Ellsworth and P.A. Reasenberg, A Brownian Model for Recurrent Earthquakes, *Bull. Seism. Soc. Am.*, 92, 2233-2250, 2002.

Nadeau, R.M., and T.V. McEvilly, Fault slip rates at depth from recurrence intervals of repeating microearthquakes. *Science*, 285, 718-721, 1999.

Nadeau, R. M. and T. V. McEvilly, Periodic Pulsing of Characteristic Microearthquakes on the San Andreas Fault, *Science*, 303, 220-222, 2004.

Scholz, C. H., The mechanics of earthquakes and faulting, *Cambridge Univ. Press, Cambridge*, 439 pp., 1990.

Working Group on California earthquake Probabilities (WGCEP). Earthquake probabilities in the San Francisco Bay Region: 2000 to 2030—a summary of findings, *U.S. Geol. Surv. Open-File Rept. 99-517*, 36 pp., 1999.

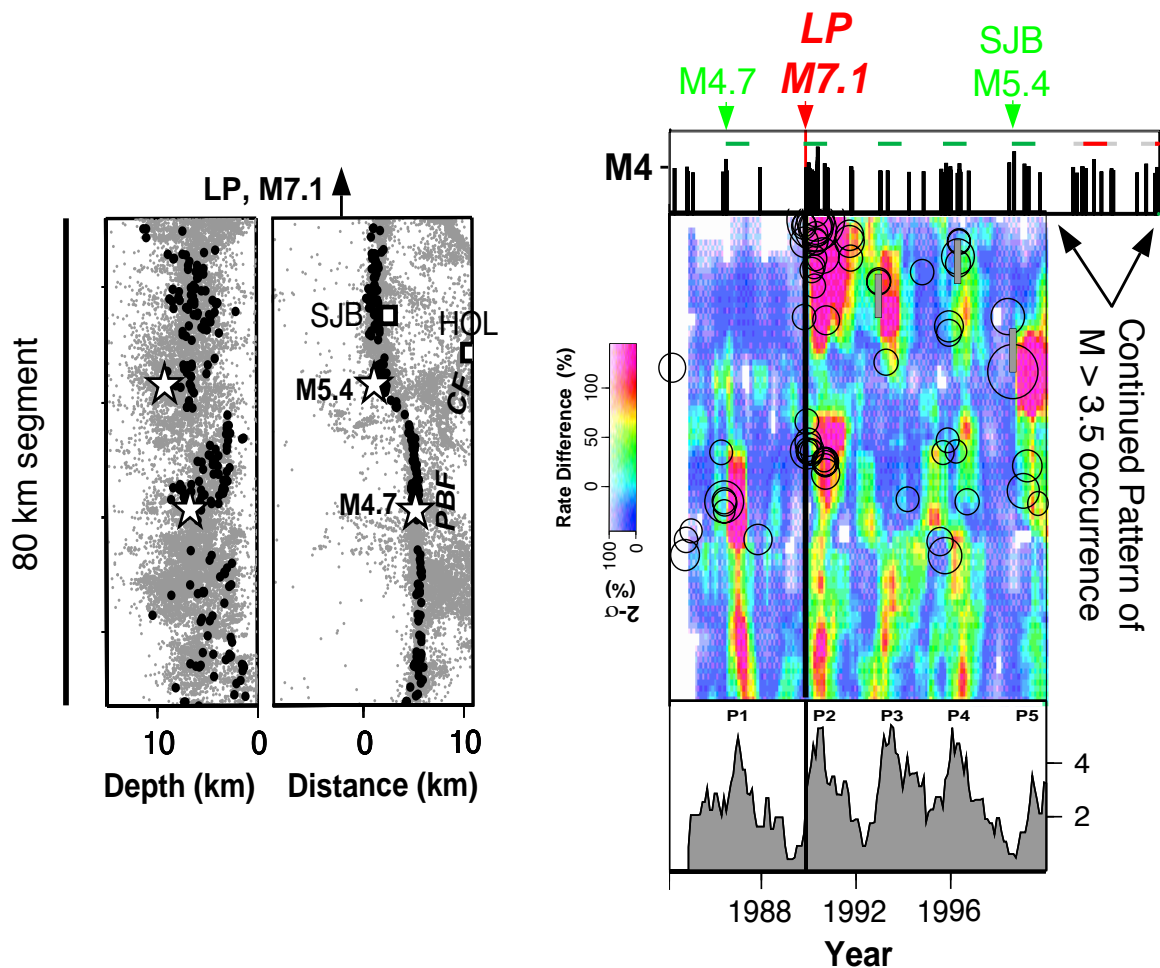


Figure 12.1: (Left) Background Seismicity (gray points) and CS locations (black circles) in depth section and map view along the northwestern 80 km segment. Horizontal scales are exaggerated by x2. White stars are locations of the two largest non-aftershock events (M5.4 and M4.7) occurring in the region and study period. Squares labeled SJB and HOL are the cities of San Juan Bautista and Hollister, CA. Calaveras and Paicines-San Benito fault seismicity are labeled CF and PBF, respectively. CS locations in map view outline the trend of the SAF. The 1989, M7.1 Loma prieta earthquake occurred adjacent to the northwest of this 80 km segment. (Right, center) Profile of the 1984-1999 (inclusive) deep slip rate history for the segment inferred from the CS data. Rates (in color) are given in percent difference from the 1984-1999 average rate and color intensity are 95% confidence bounds. Open circles are along fault positions and times of the $M > 3.5$ earthquakes occurring in the region and study period. Sizes of these circles are keyed to there relative magnitudes. Vertical black line indicates the time of the Loma Prieta earthquake. (Right, bottom) Deep slip rates as a function of time for a representative 15 km sub-segment showing the P1 through P5 pulses discussed in the text. Vertical scale is in cm/yr. (Right, top) Occurrence times and magnitudes of the $M > 3.5$ earthquakes occurring in the study zone and for the period between 1984 and 2004.73 (inclusive). The times of the Loma Prieta and two largest non-aftershock events are labeled at the top. Horizontal green bars are the pulse onset periods discussed in the text. Horizontal red bars are the projected pulse onset times based on the 1984-1999 CS slip patterns. Gray extensions of the red bars show uncertainties in these projections based on the variance of the 1984-1999 pulse recurrence intervals. Analysis of the CS data for deep slip estimation has yet to be carried out for the 2000-2004.73 time period, but the ongoing pattern of occurrence of $M > 3.5$ earthquakes suggests that the quasi-periodic deep slip pattern may also continue.

2. Finite-Source Modeling of the 22 December 2003 San Simeon Earthquake

Douglas Dreger

2.1 Introduction

The M_w 6.5 San Simeon earthquake, which occurred in the central California Coast Ranges on December 22, 2003 was analyzed with our automated finite-source procedure the day of the earthquake. The derived source information was used to incorporate rupture finiteness into the ShakeMap greatly improving its representation of near-fault ground motions as well as those in the heavily struck community of Paso Robles, about 35 km to the SE of the earthquake.

In this report the initial line-source modeling, and its application toward improving published ShakeMaps is described. In addition, the current preferred model that combines GPS and seismic waveform data is presented, and the implications of the model in terms of central Coast Range ground motion hazard is discussed.

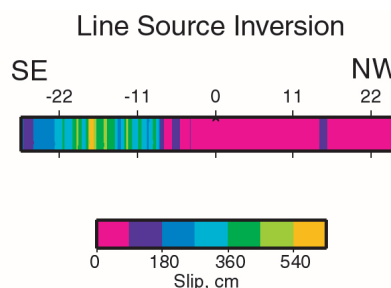
2.2 Line Source Modeling and ShakeMap

The seismic moment tensor was obtained automatically and the reviewed results were emailed within an hour after the event. The moment tensor result upward revised the magnitude from M_L 6.4 to M_w 6.5. The ShakeMap was updated with the new value automatically.

Subsequent analysis focussed on inverting broadband waveform data from the BDSN to test the two moment tensor nodal planes to determine the orientation of the causative fault. The method employed is based on *Hartzell and Heaton's* (1983) inverse scheme for kinematic rupture parameters such as slip distribution, slip rise time and rupture velocity. *Dreger and Kaverina* (2000) showed that it was possible to use a similar approach to determine key finite-source parameters quickly after an earthquake using the near-realtime broadband data stream. The *Dreger and Kaverina* (2000) method was developed by modeling the 1992 M_w 7.3 Landers and M_w 6.7 Northridge earthquakes. Although the system was not yet automated its application at the time of the Hector Mine earthquake, M_w 7.1, showed that the approach was feasible in the short time frame required for emergency response applications. The application of this method in the 2003 San Simeon earthquake is the first "live fire" test of the system, and the first time that near-realtime finite-source information was used to update ShakeMap (see *Hardebeck et al.*, 2004).

The first stage of the *Dreger and Kaverina* (2000) method is to test line-source models with the orientations of the two moment tensor nodal planes. In this analy-

sis the east dipping plane (strike=290, dip=56, rake=74) was found to fit the broadband data slightly better, though it could not be shown to be a statistically significant improvement in fit. Aftershocks, however, confirmed that the east dipping nodal plane was the causative structure. The line-source inversion results for both planes indicated that the main slip was located substantially SE of the hypocenter, extending as much as 20 km to the SE. Figure 12.2 shows the analyst reviewed line-source model for the east-dipping mechanism.



A line source inversion of broadband displacement waveforms shows that the bulk of slip is located south of the epicenter (0 on the above plot). This model assumes a rupture velocity of 2.7 km/s, and the focal parameters: strike=290, dip=56, rake=74.

Figure 12.2: Analyst reviewed line-source model of the 2003 San Simeon earthquake

The line-source information was used to incorporate source finiteness into the ShakeMap (Figure 12.3). In this calculation the distance used to model the ground motion attenuation, in areas where actual ground motion data was not available, was the closest distance to the extended fault rupture rather than to the epicenter as is typically done. The effect of this modification is an extension of the near-fault area of strongest shaking to the SE, elevating estimated ground motions in the Paso Robles region to instrumental intensity VII-VIII. This intensity is more consistent with the observed damage in the region. (e.g. *Hardebeck et al.*, 2004).

In Figure 12.3 it is shown how the ShakeMaps vary as additional information is added. Figure 12.3a shows the original ShakeMap. This map has only a few contributing stations, which are located far from the event and the afflicted region. The distribution of instrumental intensity therefore tends to be centered on the epicenter with radial decay. Estimated intensity in the vicinity of

Paso Robles is only V-VI. Figure 12.3b shows the map after adjustment by adding the finite-source information. Several days after the event as additional near-fault, non-realtime, ground motion recordings became available the ShakeMap was updated. Figure 12.3c shows the map obtained with the additional ground motion information. Note how the maps in Figures 12.3b and 12.3c agree. The former has no near-fault data, but does have the finite-rupture information obtained by inverting regional data for the rupture process, and the latter includes only the additional near-fault recordings. This comparison demonstrates the utility of incorporating either rupture finiteness or even directivity information in ShakeMaps to improve performance in regions where there may be few strong motion records or cases in which the near-fault data may not be immediately available. Finally, Figure 12.3d shows the final ShakeMap that includes all available near-fault observations as well as the finite extent of the rupture.

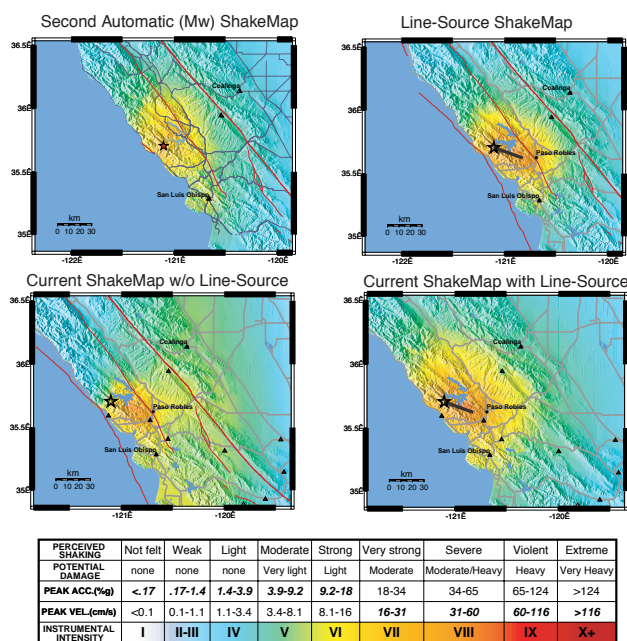


Figure 12.3: Evolution of instrumental intensity ShakeMaps (Wald et al., 1999) for the 2003 San Simeon earthquake. The star shows the epicenter, triangles the stations used, and thick line the finite extent of rupture. A), upper left, initial map based on M_w and realtime data. B), upper right, modification accounting for rupture finiteness. C), lower left, map with all available data including non realtime data. D), lower right, preferred map that combines available data and rupture finiteness.

2.3 Combined Slip Model and Ground Motion Simulation

Three-component displacement data at 8 regional and local stations, and three-component velocity records at the Parkfield site (PKD) were combined with 36 GPS permanent ground deformation vectors to invert for the detailed kinematic rupture process. This data is described in detail in Chapter 12. Figure 12.7 shows the fit to the seismic waveform data, and Figure 12.8 shows the fit to the GPS vectors. The fit to both data sets is very good. Figure 12.4. shows the slip distribution that was obtained.

The slip in the San Simeon earthquake is unusual in three respects. First, the distribution is elongated along strike, extending as much as 20 to 25 km SE of the hypocenter. This is in contrast to the primarily updip rupture of other reverse mechanism events such as the 1971 San Fernando (Heaton, 1982) and 1994 Northridge (Dreger, 1997) earthquakes. The San Simeon earthquake is similar to the much larger 1999 M_w 7.6 Chi-Chi, Taiwan earthquake in terms of the extensive along strike rupture. Secondly for a M_w 6.5 event the peak and average slip is high. Although, the peak slip is dependent upon the weight of the smoothing that is applied, all of the models show that over much of the fault the slip is between 1-3 m. Empirical relationships for average slip as a function of moment indicate that on average M_w 6.5 events have about 70 cm of average slip (e.g. Somerville et al., 1999). Third the event also has a relatively long slip rise time function that is variable over the rupture surface with an average of about 3 seconds. On average M_w 6.5 events have an average rise time of about 0.8 seconds (Somerville et al., 1999).

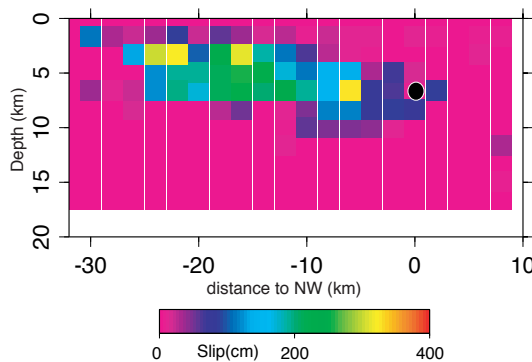


Figure 12.4: Fault normal projection of slip distribution. The black circle marks position of the hypocenter. The Fault orientation and slip vector are the same as obtained from the moment tensor analysis and used in the line-source calculation.

2.4 Central Coast Ground Motion Hazard Implications

From the derived kinematic source description it is possible to spatially and temporally integrate the slip using near-fault Green's functions to predict the distribution of near-fault strong shaking (Dreger and Kaverina, 2000). Figure 12.5a shows the results of such a calculation. The plot clearly shows the southeastward extension of ground motion contours due to the source finiteness and directivity. The two lobes of elevated ground velocity extending due east and due south of the earthquake are the directivity-amplified SH lobes of the reverse mechanism.

Whether the observed ground motions from the 2003 M_w 6.5 event are representative of all central Coast Range magnitude 6.5 earthquakes is an important question. There are strike-slip faults in the region, and the last large nearby earthquake, the 1952 Bryson event, was predominantly strike-slip (Dehlinger and Bolt, 1987). In order to address this question the kinematic source description that was obtained for the 2003 San Simeon earthquake was used to simulate near-fault ground motions for a hypothetical vertically dipping right-lateral strike-slip fault. The results of the calculation shows that for the vertical strike-slip fault the effect of directivity is greatly enhanced. In some areas the peak ground velocity can be three times greater, and the area receiving greater than 10 cm/s is four times larger than the reverse slip case. Fortunately in the 2003 San Simeon earthquake the slip direction was perpendicular to the rupture direction producing a relatively mild directivity effect. These calculations show however that while the recorded ground motions from the 2003 San Simeon earthquake are useful for characterizing earthquake hazard in the central Coast Ranges similar sized strike-slip earthquakes could be significantly more damaging.

2.5 References

Dehlinger, P., and B. Bolt, Earthquakes and associated tectonics in a part of coastal central California, *Bull. Seis. Soc. Am.*, 77, 2056-2073, 1987.

Dreger, D. S. The large aftershocks of the Northridge earthquake and their relationship to mainshock slip and fault-zone complexity, *Bull. Seism. Soc. Am.*, 87, 1259-1266, 1997.

Dreger, D., and A. Kaverina, Seismic remote sensing for the earthquake source process and near-source strong shaking: A case study of the October 16, 1999 Hector mine earthquake, *Geophys. Res. Lett.*, 27, 1941-1944, 2000.

Hardebeck, J.L., J. Boatwright, D. Dreger, R. Goel, V. Graizer, K. Hudnut, C. Ji, L. Jones, J. Langbein, J. Lin, E. Roeloffs, R. Simpson, K. Stark, R. Stein, J.C. Tinsley, Preliminary report on the 22 December 2003, M 6.5 San Simeon, California earthquake *Seism. Res. Lett.*, 75, 155-172, 2004.

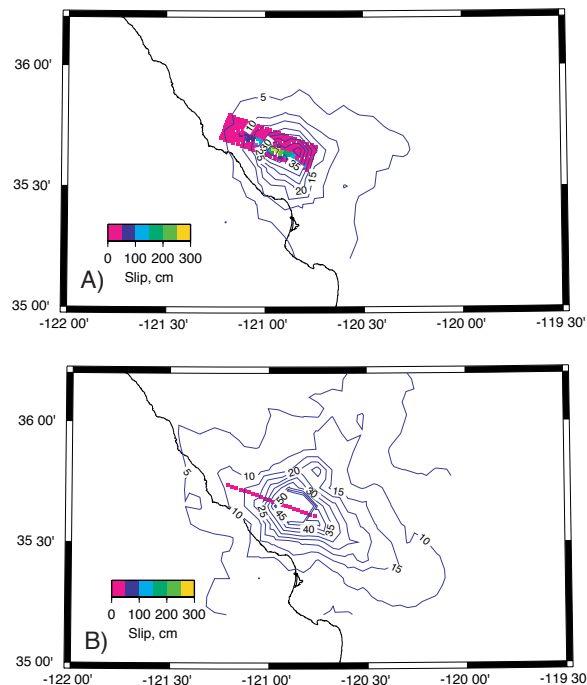


Figure 12.5: Simulated peak ground velocity assuming the obtained kinematic source description. Contours are in intervals of 5 cm/s beginning with 5 cm/s. The surface projection of slip is shown. A) Simulated PGV for the actual reverse slip mechanism. B) Simulated PGV for a vertical right-lateral strike-slip mechanism.

Hartzell, S. H., and T. H. Heaton, Inversion of strong ground motion and teleseismic waveform data for the fault rupture history of the 1979 Imperial Valley, California, earthquake, *Bull. Seism. Soc. Am.*, 73, 1553-1583, 1983.

Heaton, Y. H. The 1971 San Fernando earthquake: a double event?, *Bull. Seism. Soc. Am.*, 72, 2037-2062, 1982.

Somerville, P. G., K. Irikura, R. Graves, S. Sawada, D. Wald, N. Abrahamson, Y. Iwasaki, T. Kagawa, N. Smith, and A. Kowada. Characterizing crustal earthquake slip models for the prediction of strong ground motion, *Seism. Res. Lett.*, 70, 59-80, 1999.

Wald, D. J., V. Quitoriano, T. H. Heaton, H. Kanamori, C. W. Scrivner, and C. B. Worden. TriNet ShakeMaps: Rapid generation of instrumental ground motion and intensity maps for earthquakes in southern California, *Earthquake Spectra*, 15, 537-555, 1999.

3. Coseismic Slip Distribution of the 22 December 2003 San Simeon Earthquake

Frédérique Rolandone, Roland Bürgmann, Doug Dreger, and Mark Murray

3.1 Introduction

The M_w 6.5 San Simeon earthquake struck the central California coast on December 22 2003, 50 km west of the San Andreas fault. The San Simeon earthquake is one of several destructive blind-thrust earthquakes to have hit the central California Coast Range during the past two decades. This thrust earthquake accommodates a compressional component of the Pacific-North America plate motion. The mainshock nucleated at a depth of 8 km and was followed by a vigorous aftershock sequence primarily southeast of the hypocenter, consistent with the mainshock directivity (Hardebeck *et al.*, 2004). The strong directivity of the rupture resulted in a concentration of damage to the southeast, with high levels of damage in Paso Robles.

We combine geodetic and seismic data sets to constrain the coseismic slip distribution of the San Simeon earthquake. We use continuous and survey-mode GPS observations along with seismic waveform data from the Berkeley Digital Seismic Network (BDSN/CISN). We invert both data sets for fault slip model. Seismic and geodetic data sample ground deformation at different time scales and combining them provide more stable results than the inversion from individual data sets. The inversion results for this event indicate that the slip extend to the southeast of the epicenter approximately 25 km and in a depth range between 1.3 and 8 km.

3.2 GPS Data and Analysis

We use data from 36 GPS sites in this study. The San Simeon earthquake produced static displacements at 14 continuously operating GPS stations located within 70 km of the epicentral region. These stations are located northeast of the rupture near the Parkfield segment. The cluster of stations near Parkfield were displaced southwest by about 15 mm. One station 35 km northwest of the rupture moved about 60 mm southwest. In addition, one continuous station south of the rupture and 4 continuous stations north of it (operated by the University of Wisconsin since January 2003) recorded small (less than 12 mm) displacements.

Many of the 17 survey-mode GPS sites are located within 40 km of the rupture and provide useful coseismic deformation signals. Following the San Simeon earthquake, we resurveyed 6 GPS stations northeast of the mainshock. The USGS began continuously occupying 3 stations west of the epicenter one day after the event and another site southeast of the mainshock one week

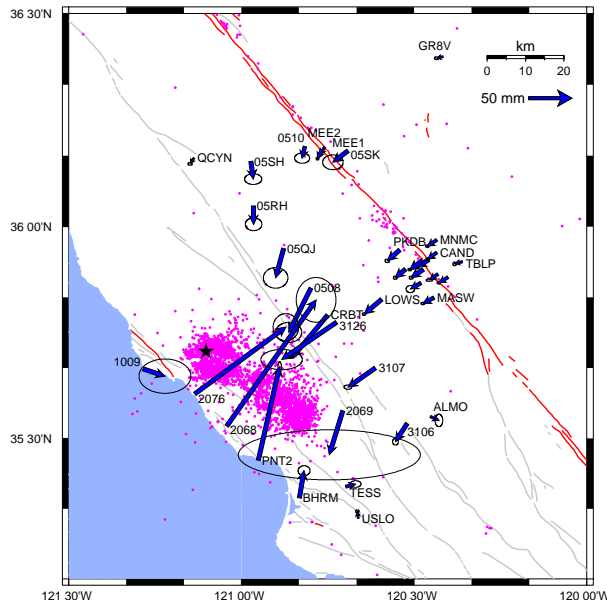


Figure 12.6: GPS sites and coseismic displacements from the M_w 6.5 San Simeon earthquake with 95% confidence ellipses. The black star shows the epicenter, the pink dots show relocated aftershocks (Hardebeck *et al.*, 2004). Surface fault traces are shown as red and grey lines.

later. Three sites east of the rupture were occupied by JPL within 3 days of the event. A survey of 4 additional sites south of the rupture was done 2 months after San Simeon.

For the campaign GPS sites, we have pre-existing GPS observations collected since the mid-1980's. Some of the sites have multiple years of measurements prior to the earthquake and have precise velocities. For the sites with less than 3 campaigns of data, we use interseismic velocities from the SCEC Crustal Motion Map (CMM). The CMM velocities indicate that the epicentral region had a well-constrained secular deformation field, which allows coseismic displacements to be reliably estimated from pre- and post-event measurements. We use the GAMIT/GLOBK GPS processing software to analyze the GPS data and combine our daily solutions and an appropriate set of global and regional solutions from SOPAC. We estimated the coseismic offsets at each site from these time series assuming that the interseismic velocity is the same before and after the earthquake. The southwest sites, closest to the rupture, recorded larger

coseismic offsets than the northeast sites (Figure 12.6). The largest measured horizontal displacement was 179 ± 14 mm.

3.3 Geodetic and Seismic Data Inversion for Fault Slip Model

We use the geodetic data to constrain the rupture geometry. We model the observed coseismic displacements using rectangular dislocations in an elastic, homogeneous and isotropic half-space (Okada, 1985). We use a constrained, nonlinear optimization algorithm (Bürgmann *et al.*, 1997), which allows us to estimate the geometry (parameterized by length, depth, width, dip, strike, and location) and the strike-slip and dip-slip offsets of one fault that best fit the GPS data. The optimal fault model has a strike of 303° and dips 56° to the northeast.

We use the results of our geometry inversion to construct the north-dipping fault plane to determine the distribution of fault slip. Our best-fitting single-fault model is enlarged at the down-dip and lateral edges and discretized into 2 by 2 km elements for the distributed slip inversions. We find that the optimal uniform-slip dislocation is consistent with seismological evidence. The San Simeon focal mechanism and the aftershock distribution suggest the Oceanic fault as the main rupture zone (Hardebeck *et al.*, 2004). The oceanic fault has a strike of about 292° near the epicenter and changes direction to the south with a more northern strike similar to the one given by our geometry inversion. Our measure of misfit, the reduced χ^2 value, is not improved if we allow for a second dislocation in the geometry inversion.

We combined displacement and velocity waveform data from 9, three-component BDSN/CISN strong motion stations with 36 observations of GPS deformation to simultaneously invert for the distribution of fault slip. The waveform data was processed by deconvolving the instrument response, double integrating the recorded acceleration to displacement (PKD was integrated only to velocity), and high pass filtering above 0.01 Hz to remove long-period noise.

The seismic waveform data may be generally characterized as low-frequency (Figure 12.7) and in order to model this characteristic a multiple time window approach (e.g. Hartzell and Heaton, 1983; Dreger and Kaverina, 2000; Kaverina *et al.*, 2001) was used to resolve the slip rise time distribution of the rupture. The results of the inversions indicate that the rise time was relatively long for a M_w 6.5 event with an average of about 3 seconds. The rupture velocity, though not well resolved, was found to be 2.6 km/s. Consistent with the non-linear GPS inversions for fault orientation the combined inversion favors a more northerly striking fault plane (strike=303, dip=56). The resulting slip model is shown in Figure 12.8. The slip is found to be shallow in depth (1.3 to 8 km) and extends approximately 25 km to the southeast of the epi-

center. This unusual aspect ratio for reverse fault rupture is consistent with the results of separate GPS and seismic waveform inversions, and leads to a moderate horizontal directivity effect as compared to a more typical updip directivity as was observed in the 1994 Northridge, California earthquake. The spatially concentrated peak slip was found to be 5.5 m, which is unusually high for a M_w 6.5 event, and it does depend on the applied smoothing. Over much of the fault, however the slip is between 1 to 3 m. The level of fit to the GPS and seismic waveform data is excellent as shown in Figure 12.7 and 12.8.

The extension of slip to the southeast of the epicenter indicates that this event ruptured unilaterally to the southeast producing a pronounced directivity effect in that direction. Elevated ground motions in the Paso Robles region, about 35 km to the southeast, resulted in two deaths from collapsed unreinforced masonry (URM) buildings, and numerous damaged red-tagged URM buildings in Paso Robles.

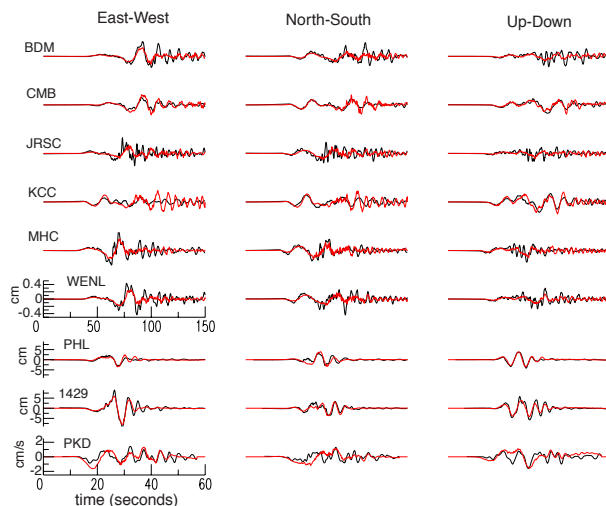


Figure 12.7: Comparison of observed (black) and simulated (red) displacement waveforms (velocity for PKD) for the combined seismic waveform and GPS model. Quantitatively the fit to the data was found to be excellent with a 72% variance reduction.

3.4 References

- Bürgmann, R., P. Segall, M. Lisowski, and J. Svarc, Postseismic strain following the 1989 Loma Prieta earthquake from GPS and leveling measurements, *J. Geophys. Res.*, 102, 4933-4955, 1997.
- Dreger, D., and A. Kaverina, Seismic remote sensing for the earthquake source process and near-source strong shaking: A case study of the October 16, 1999 Hector mine earthquake, *Geophys. Res. Lett.*, 27, 1941-1944, 2000.

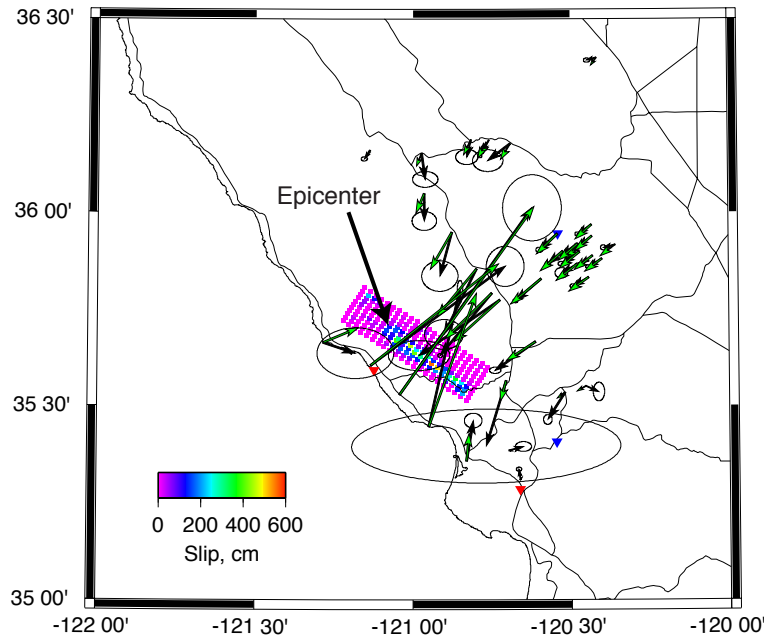


Figure 12.8: Map showing the surface projection of slip from the combined inversion. The epicenter is located at the northwestern edge of the slip distribution. Observed (black) and predicted (green) gps vectors are also shown. For reference major highways are also plotted. Quantitatively the fit to the GPS data was found to be excellent with a 94% variance reduction. A color version of this figure may be found on page 104.

Hardebeck, J.L., J. Boatwright, D. Dreger, R. Goel, V. Graizer, K. Hudnut, C. Ji, L. Jones, J. Langbein, J. Lin, E. Roeloffs, R. Simpson, K. Stark, R. Stein, J.C. Tinsley, Preliminary report on the 22 December 2003, M 6.5 San Simeon, California earthquake *Seism. Res. Lett.*, 75, 155-172, 2004.

Hartzell, S. H., and T. H. Heaton, Inversion of strong ground motion and teleseismic waveform data for the fault rupture history of the 1979 Imperial Valley, California, earthquake, *Bull. Seism. Soc. Am.*, 73, 1553-1583, 1983.

Ji, C., K.M. Larson, Y. Tan, K.W. Hudnut, and K. Choi, Slip history of the 2003 San Simeon Earthquake constrained by combining 1-Hz GPS, strong motion, and teleseismic data, submitted, 2004.

Kaverina, A., D. Dreger and E. Price. The combined inversion of seismic and geodetic data for the source process of the 16 October 1999 M_w 7.1 Hector Mine, California, earthquake, *Bull. Seism. Soc. Am.*, 92, 1266-1280, 2002.

Okada, Y., Surface deformation due to shear and tensile faults in a half-space, *Bull. Seism. Soc. Am.*, 75, 1135-1154, 1985.

4. Measuring and Modeling Fluid Movements in Volcanoes: Insights from Continuous Broadband Seismic Monitoring at Galeras Volcano, Colombia

Margaret Hellweg, Leigh House (Los Alamos National Laboratory) and Douglas Dreger

4.1 Introduction

One important goal of volcano monitoring is to be able to reliably identify significant changes in a volcano's activity, in order to minimize the threat to the local population and infrastructure. Seismic signals are often the most immediate indicators of such changes (*McNutt, 1996*), and to interpret them, we must understand the processes which produce them. At volcanoes, we observe two basic types of seismic signals. Volcano-tectonic events are earthquakes, usually small ones, resulting from slip across fault planes. The second type of events are non-tectonic and are unique to volcanoes. They include volcanic tremor, long period (LP) events, and less commonly, tornillos. In seismic recordings, non-tectonic signals are often emergent, may continue for a long time, and have highly variable amplitudes. Very often their spectra contain one or a few distinct, sharp peaks. They are assumed to be associated with the movement of fluids in the volcanic system (for a review, see *Konstantinow and Schlindwein, 2002*).

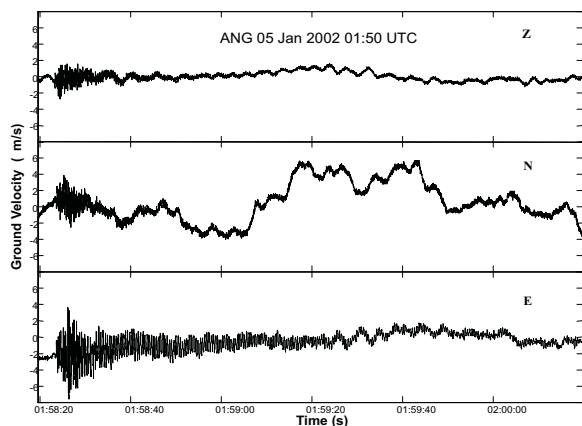


Figure 12.9: Unfiltered three-component record of a tornillo recorded at the crater rim seismic station ANG. The coda of the E component bears the most resemblance to a screw. The very long period noise particularly apparent on the N component is most likely due to wind.

4.2 Tornillos

At Galeras Volcano, Colombia, ‘tornillos’ occurred prior to explosive eruptions in 1992 and 1993 (*Narvez et al, 1997*). These distinctive seismic events have identifiable onsets and relatively long, gradually decaying event tails (codas) and their name comes from the resemblance of their shape on the seismic record to a screw (Spanish: tornillo. Figure 12.9). Their spectra have one or a few narrow peaks. That is, they are monochromatic or multi-chromatic (Figure 12.10). From December 1999 to December 2002, ninety tornillos occurred at Galeras Volcano, Colombia, and were recorded with broadband, three-component seismometers (*Seidl et al, 2003*). These tornillos have between 1 and 15 spectral peaks. To characterize the tornillos and learn what causes them, we are investigating the coda which gives them their name. The analysis of the coda follows the procedure described by *Seidl and Hellweg (2003)*, where each spectral peak in each tornillo is treated separately. Based on the azimuth Az_n , inclination In_n and rectilinearity Re_n for each spectral peak, the seismograms are rotated from the Z-N-E coordinate system of the seismometer into a coordinate system of the wavefield, X1-X2-X3. From these records, the frequency of the peak's maximum, f_{Pn} , and its amplitude, AP_n , are measured in the frequency domain, while the maximum velocity amplitude, v_n , damping factor, Q_n and the signal energy, EP_n , are measured in the time domain.

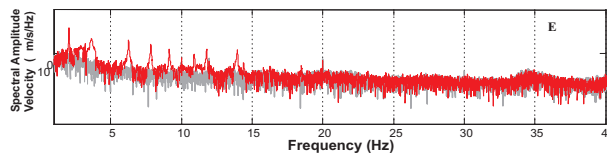


Figure 12.10: Linear-logarithmic spectrum of the E component for the tornillo shown in Figure 12.9. The spectrum during the tornillo is superimposed on the spectrum of the seismic noise before the tornillo (gray). Note the extremely narrow spectral peaks between 1 and 15 Hz.

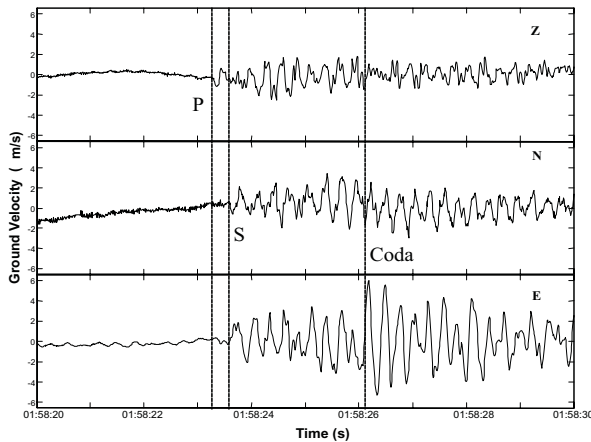


Figure 12.11: Expanded seismograms for the beginning of the tornillo shown in Figure 12.9. These data have been bandpass filtered between 1 and 40 Hz to suppress long-period noise. Note the clear onset on the vertical component marked P and the onsets on the horizontal components 0.25 s later marked S. It takes a little over 2 s for the characteristic coda of the tornillo to develop.

4.3 Interpretation

For the characteristic coda of the tornillos, it is clear that the frequencies of the spectral peaks present, which may range from 1 Hz to 40 Hz, are related to the source, but we have not yet found a pattern allowing us to predict precisely which frequencies or families of frequencies will be present in any particular tornillo. For the spectral peaks below 5 Hz, the polarization both remains constant during an individual tornillo and varies little from one tornillo to the next. This suggests that tornillos are all generated within a limited volume of the volcanic edifice. The variation in the polarization at higher frequencies should allow us to constrain the size of this volume (Hellweg, 2003). With the high resolution data from broadband instruments, we can see that the onset of the tornillo is small but clearly impulsive (Figure 12.11). The initial P-pulse on the vertical component is followed 0.25 s later by S-waves on the horizontal components. A transition of about two seconds follows before the characteristic coda develops. As we determine details about the tornillo onset and this intermediate wavepacket, and their relationships to the characteristics of the tornillo coda, we shall be able to derive a more thorough picture relating the triggering mechanism to its effect on the coda.

4.4 Acknowledgements

This project is funded by U.C. Berkeley - Los Alamos National Laboratory collaborative Institute for Geo-

physics and Planetary Physics Project number 04-1407. Tornillo data have been acquired as part of a cooperative project between the Bundesanstalt für Geowissenschaften und Rohstoffe (Germany) and the Instituto de Investigación e Información Geocientífica Minero-Ambiental y Nuclear (Colombia) on Multiparameter Monitoring of Volcanoes.

4.5 References

- Hellweg, M., The Polarization of Volcanic Seismic Signals: Medium or Source?, *J. Volc. Geotherm. Res.*, *128*, 159-176, 2003.
- Konstantinou, K.I. and V. Schlindwein, Nature, wavefield properties and source mechanism of volcanic tremor: a review. *J. Volcanol. Geotherm. Res.*, *119*, 161-187, 2002.
- McNutt, S.R., Seismic monitoring and eruption forecasting of volcanoes: A review of the state-of-the-art and case histories. In: *Monitoring and Mitigation of Volcano Hazards* (Eds. Scarpa, R. and Tilling, R.I.), Springer, Berlin-Heidelberg, 100-146, 1996.
- Narváez, M.L., R.A. Torres, D.M. Gómez, G.P.J. Cortés, H.V. Cepeda, and J. Stix, Tornillo-type seismic signals at Galeras volcano, Colombia, 1992-1993. *J. Volcanol. Geotherm. Res.*, *77*, 159-171, 1997.
- Seidl, D., M. Hellweg, M. Calvache, D. Gómez, A. Ortega, R. Torres, F. Böker, B. Buttkus, E. Faber and S. Greinwald, The multiparameter-station at Galeras Volcano (Colombia): Concept and realization, *J. Volc. Geotherm. Res.*, *25*, 1-12, 2003.
- Seidl, D. and M. Hellweg, Parametrization of multichromatic tornillo signals observed at Galeras Volcano (Colombia), *J. Volc. Geotherm. Res.*, *125*, 171-189, 2003.

5. The Orinda Earthquake Sequence

Margaret Hellweg

5.1 Introduction

On October 19 and 20, 2003, two earthquakes with M_L 3.5 and M_L 3.4 occurred ENE of Orinda, CA. Fortuitously, their hypocenters were located almost directly below Berkeley Seismological Laboratory’s station at Russell Reservation Field Station, BRIB (37.92 N, 122.15 W). This station is equipped at the surface with a Guralp CMG-3T in a 35 m posthole installation and a FBA-23 accelerometer. In addition, the station has a 3-component Oyo HS-1 geophone and a 3-component Wilcoxon 731A accelerometer in a borehole at a depth of 119 m.

5.2 The Seismicity

Since it is a short-period instrument, the Oyo HS-1 geophone in the borehole at BRIB usually only records local events. In the days, leading up to October 19, 2003, there were several small earthquakes, but they belonged to a sequence in Danville/Alamo, CA, further to the south and east. The Orinda sequence began on October 19, 2003 at 14:35 UTC (07:35 PDT) with an earthquake with M_d 2.5. This event was followed by more than 15 smaller events, the largest of which, at 15:12 UTC with M_d 1.67, was also located. Just under one hour later, a larger earthquake occurred, the M_L 3.5 mainshock of the sequence.

The two largest earthquakes, the mainshock at 15:32 UTC on October 19 with M_L 3.5, and the aftershock at 17:50 on October 20 with M_L 3.4, were clipped on one of the horizontal components of both the surface and the borehole seismometers. Fortunately, the clipped component of the borehole seismometer coincides with the single functioning component of the borehole accelerometer. When the instrument response is removed from the accelerometer recording and the trace is integrated, it matches the corresponding component of the velocity sensor. Figure 12.12 shows the three component recording of the mainshock, with the vertical trace at the top and the two orthogonal horizontal traces (H1 and H2) below. The bottom trace (H2) was clipped in the velocity recording and has been replaced by the integrated accelerometer trace. The offset traces between 15:32:50 and 15:32:53 are scaled 100,000 times the traces for the mainshock. There is clearly a very small event 1.5 s before the mainshock onset showing the range of sizes of the events in this sequence and the similarities in the waveform of both large and small events.

Of the many events which occurred during the first 24 hours of the sequence, only 14 appear in the catalog of the Northern California Seismic Network (NCSN)

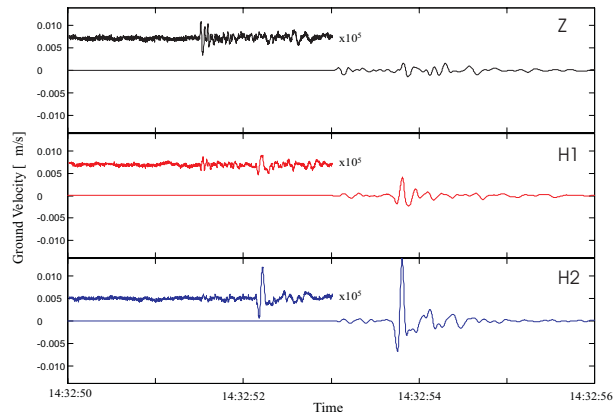


Figure 12.12: Three-component recording of the mainshock on the borehole instruments. H1 and H2 are the two orthogonal horizontal components. For this figure, the H2 recording has been replaced by the instrument-corrected and integrated record from the borehole accelerometer. The offset traces in the first 3 s of the figure have been scaled by a factor of 100,000 to show the “pre-event noise”, in this case a very small foreshock.

with locations and magnitudes. While the catalog reports depths of approximately 10 km for the two largest quakes, the S-P times at the station BRIB for all the events in the sequence range from 0.58 to 0.7 s. They must therefore be located less than 6 km below the station. The borehole instrument recorded more than 4000 fore- and aftershocks in the first week of the sequence. At the beginning of December aftershocks continued at a rate of 6 or more per day, with a M_d 2.9 aftershock recorded January 1, 2004.

Standard magnitudes cannot be determined for most of the earthquakes in the sequence: the events are too small to be recorded at other stations and, strictly speaking, the local magnitude scale is not defined for events as close as 6 km. To determine the magnitude threshold for the events, I calibrated a “manual magnitude” scale using the 14 events from the catalog. Following the definition of local magnitude (*Richter*, 1935), I measured the peak-to-peak amplitudes in the instrument-corrected velocity seismograms of the two horizontal components of the borehole velocity sensor and multiplied by the period and by the magnification of a Wood-Anderson instru-

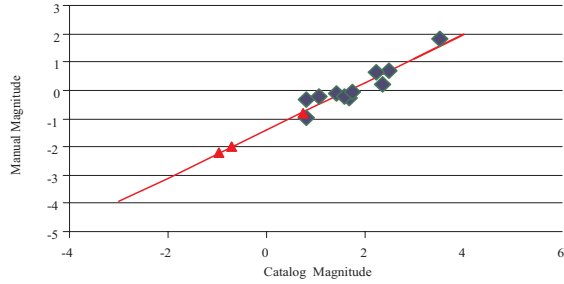


Figure 12.13: Calibration of “manual magnitude” to catalog magnitude (M_L or M_d). Diamonds denote events for which the NCSN catalog gives magnitudes. Triangles show how events for which only manual magnitudes exist. They have been placed on the regression line to determine their corresponding catalog magnitude.

ment at that period. The manual magnitude is defined as $M_m = \log_{10}[(N_{max} + E_{max})/2]$. This numerical result is comparable to the measurement used to determine M_L . As the distances of these events from the station BRIB are all nearly the same, no distance correction is necessary. Figure 12.13 shows a comparison between the catalog and manual magnitudes (diamonds). The line shows the regression using of the catalog magnitudes and manual magnitudes and allows me to project manual magnitudes to a corresponding catalog magnitude (triangles). The sequence includes still smaller events for which I have not yet determined manual magnitudes, thus the earthquakes in the sequence recorded at station BRIB range over more than 5 magnitudes in size.

5.3 Perspectives

This sequence provides a well-recorded multitude of tightly clustered, small events ranging over 5 magnitude units in size. It thus offers an excellent opportunity to investigate various aspects of event scaling and aftershock statistics.

5.4 References

Richter, C.F., An instrumental earthquake magnitude scale, *Bull. Seismol. Soc. Am.*, 25, 1-32, 1935.

6. Non-Double-Couple Earthquakes in the Long Valley Volcanic Region

Dennise C. Templeton and Douglas Dreger

6.1 Introduction

We study the extent of fluid-influenced faulting in the Long Valley volcanic region to better understand the connection between earthquake production and the geothermal and magmatic system. In the analysis of earthquake data, most events are assumed to follow the double-couple (DC) model of faulting characterized by shear along a linear fault plane induced by tectonic stresses. Earthquakes with coseismic volume changes indicate that tectonic forces were not the only factor contributing to failure. In geothermal or volcanic areas, such events are thought to be influenced by fluid migration, in either liquid or gas form, or a change in the state of matter of a fluid (Ross *et al.*, 1999 ; Dreger *et al.*, 2000).

In this study, we focus on a 100 km wide circular area centered at Long Valley caldera which encompassed the Mono-Inyo craters to the north and the Sierra Nevada mountain block to the south. A comprehensive search was performed for events greater than M3.5 since 1993 with significant non-DC components, specifically compensated-linear-vector-dipole (CLVD) and isotropic components.

6.2 Method

We model the waveforms of 128 events recorded in the NCSN catalog greater than M3.5 using four different source models: DC, DC+CLVD, DC+isotropic, and DC+CLVD+isotropic. For the DC and DC+isotropic models, a grid search method iterating over strike, dip, rake, DC moment and isotropic moment, which is equal to zero in the pure DC case, was used to find the solution which best fit the observed three-component waveforms. For the deviatoric and full moment tensor models, the second rank symmetric seismic moment tensor was solved by linearly inverting complete three-component broadband seismograms in the time domain using a weighted least squares approach. Green's functions for all four models were computed utilizing a frequency wavenumber integration method and the SoCal velocity model (Dreger and Helmberger, 1993). A set of seven BDSN stations (BKS, CMB, KCC, MHC, ORV, PKD, and SAO) providing the best azimuthal coverage and data quality were used in this investigation. In practice, however, a solution would usually have a subset of these stations in its inversion depending on station availability and data quality issues. Both data and synthetics were bandpass filtered between 0.02 and 0.05 Hz.

Using the F test as a statistical aid, we determine which of the four models was most appropriate for each

individual earthquake. Statistically significant isotropic components were determined if the improvement in fit to the data when using a more complex model was at or above the 90% significance level. We also performed several analyses to determine the stability of the solution, the depth sensitivity of the isotropic component, the recoverability of isotropic components, and the possibility of obtaining a spurious isotropic component.

6.3 Results

Within the chosen space and time constraints, 33 events were identified that had solutions with three or more stations in their inversion (Figure 12.14). Of these 33 events, 28 had statistically insignificant non-DC components. The remaining five events had statistically significant positive volumetric components. Two of these five also had statistically significant CLVD components. All of the non-DC events were located either in the south moat of the caldera or in the Sierra Nevada block. We were not able to analyze the source process of earthquakes in or near the vicinity of the Mono-Inyo volcanic chain because events greater than M3.5 were not recorded during the time interval investigated by this study.

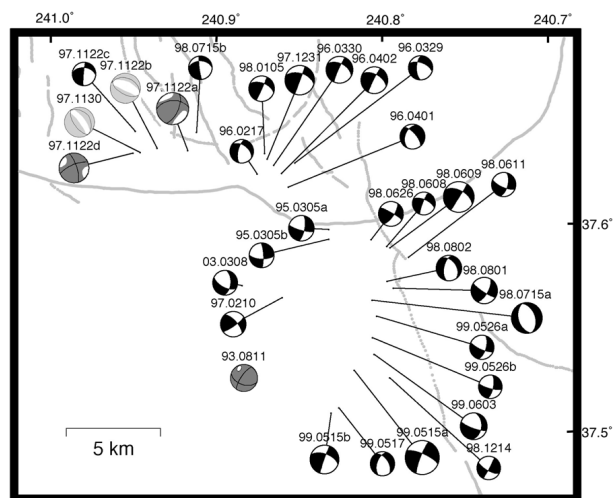


Figure 12.14: DC solutions shown in black. DC+isotropic solutions shown as dark gray. Full moment tensor solutions shown as light gray. Date of event shown as YY.MM.DD.

To test the stability of the focal mechanism solutions, we performed Jackknife tests on three events: DC event 97.12.31, DC+isotropic event 97.11.22b, and full moment

tensor event 97.11.30. Each event originally had six stations in its solution. We solve for all permutations of three, four, and five station combinations and compare these results with the six station solution for each event. DC and DC+isotropic solutions are remarkably stable for solutions with four or more stations in their inversion. Solutions with three stations in the inversion are seen to be slightly more variable. The full moment tensor event showed that the P-wave radiation pattern was stable but that the orientation of the faulting planes was unstable even when using as many as five stations. However it is important to note that the DC component of this event produced only 5% of the total moment released and that the CLVD and isotropic components dominated the inversion. Thus, inversions with four or more stations can be treated with confidence. Three station inversions, while often consistent with solutions with more stations, should be understood to have more uncertainty in the solution.

Most moment tensor inversions in this study did not have good depth control. In some cases, changes in depth may produce statistically significant isotropic components. For eight events, we test for spurious isotropic components due to depth mislocation using the station combination which yielded the best solution in each case. Solutions for source depths between 2 - 11 km are calculated for the five events with significant isotropic events and three DC events (events 97.12.31, 98.06.09, and 98.07.15a). These tests illustrate the importance of accurately knowing the depth of events when attempting to identify earthquakes with significant isotropic components. For the DC events, we can see that for depths deeper than the independently determined NCSN catalog depths, the improvement in fit to the data between the DC and DC+isotropic model is statistically significant. However, the overall fit to the data decreases with depth which indicates that the isotropic components are not modeling the true source behavior. For the DC+isotropic and full moment tensor events, solutions at depths shallower than the catalog depths sometimes do not recover the significant isotropic component. For some events depths outside the allowable range can fit the data better, however, it is important to remember that with the long wavelength data used in this study, the depth of the source is not well constrained which is why NCSN catalog depths are used as an independent constraint.

To determine the stability of the isotropic component with station combination, we performed Jackknife tests on the four events with significant isotropic components that had four or more stations in their inversion. For each event, for all station combinations of three or more, we determined the statistical significance of the volumetric component. For all events, all combinations of four or more stations recovered the statistically significant

isotropic component. For solutions with three station in the inversion, only four permutations out of 70 failed to recover the isotropic component. It is reasonable to assume that significant isotropic components can be recovered with as few as three, but preferably with at least four, stations in the inversion. Thus, we can be confident that there are no false negative occurrences within my set of 33 events.

We also investigate the possibility of obtaining a spurious isotropic component due to poor data coverage. For this test, we take three high quality DC inversions (events 97.12.31, 98.06.09, and 98.07.15a) and perform Jackknife tests to see if any combination of three or more stations would result in a statistically significant isotropic component at or above the 90% significance level. For their best solutions, events 97.12.31 and 98.06.09 had six stations in their inversions and event 98.07.15a had seven stations in its inversion. Of 65 four station inversions, four returned a false positive. Of 75 three station inversions, six returned a false positive. Five and six station inversions did not return false positives. Thus, from these tests, events with significant isotropic components that have four or fewer stations in their inversion should be treated with caution. This test casts doubt as to the validity of event 93.08.11 which has only three stations in its inversion.

6.4 Acknowledgements

We appreciate support for this project by NSF through contracts EAR-0087147 and EAR-0105998.

6.5 References

- Dreger, D.S. and D.V. Helmberger, Determination of source parameters at regional distances with three-component sparse network data, *J. Geophys. Res.*, *98*, 8,107 - 8,125, 1993.
- Dreger, D. S., H. Tkalic, and M. Johnston, Dilational processes accompanying earthquakes in the Long Valley Caldera, *Science*, *288*, 122 - 125, 2000.
- Ross, A., G. R. Foulger, and B.R. Julian, Source processes of industrially-induced earthquakes at The Geysers geothermal area, California, *Geophysics*, *64*, 1,877 - 1,889, 1999.

7. Observations of Infragravity Waves at the Monterey Ocean Bottom Broadband Station (MOBB)

David Dolenc and Barbara Romanowicz

7.1 Introduction

Ocean bottom broadband seismic observations show increased noise level when compared to land recordings. Infragravity waves are an important source of background noise at periods longer than 20 seconds. Long-period background noise can partially be removed by post-processing (Crawford and Webb, 2000; Stutzmann *et al.*, 2001). At the same time, observations of infragravity waves can help us better understand their generation from short-period waves. We investigated correlations between the infragravity waves recorded at MOBB and the short-period ocean wave data recorded at nearby ocean buoys. MOBB was installed 40 km offshore in the Monterey Bay at a water depth of 1000 m in April 2002 in collaboration between Berkeley Seismo Lab and Monterey Bay Aquarium Research Institute (MBARI) (McGill *et al.*, 2002; Uhrhammer *et al.*, 2002). It comprises a three-component broadband seismometer with a temperature sensor, a water current meter measuring current speed and direction, and a differential pressure gauge (DPG). The station is continuously recording data which are retrieved, on average, every three months.

7.2 Results

We calculated power spectral density (PSD) of the MOBB vertical component for 1-hour long periods for all the data recorded until February 2004. The results were compared to the spectral wave density (SWD) of the ocean waves as recorded on the eight NOAA buoys located from offshore Southern California to Alaska. The results clearly showed that the width of the infragravity wave band recorded on MOBB was best correlated with the energy of the ocean waves recorded at the local NOAA buoy 46042, located just 23 km W of MOBB. To further explore observed correlation between the MOBB PSD and the buoy SWD, we focused on a 7-day period and included 6 more buoys that were closest to MOBB, and had data available. We calculated correlation coefficient between 1-hour long MOBB PSD and buoy SWD values. Results for 5 of the buoys are presented in Figure 12.15. The highest correlation can be observed for the closest buoy (46042). The result also shows that the 7-17 sec ocean waves are best correlated with seismic waves with 30-200 sec period. A weaker correlation can be observed with the other two buoys located over the continental shelf to the north (46012 and 46014). Correlation with the buoy located to the south (46011) and the one further offshore (46059) is much smaller. We plan to

further investigate these observations as well as include pressure and tides data to better understand where and how the energy is transferred from the ocean to the seismic waves. Once the reliable DPG data from the MOBB are available we will also use them to remove the long-period noise from the MOBB vertical channel to improve the seismic data quality.

7.3 References

Crawford, W.C., and S.C. Webb, Identifying and removing tilt noise from low-frequency (<0.1 Hz) seafloor vertical seismic data, *Bull. Seism. Soc. Am.*, 90, 952-963, 2000.

McGill, P., D. Neuhauser, D. Stakes, B. Romanowicz, T. Ramirez, and R. Uhrhammer, Deployment of a long-term broadband seafloor observatory in Monterey Bay, *EOS Trans. Amer. Geophys. Un.*, 83, F1008, 2002.

Stutzmann, E., J.-P. Montagner, A. Sebai, W.C. Crawford, J.-L. Thiot, P. Tarits, D. Stakes, B. Romanowicz, J.-F. Karczewski, J.-C. Koenig, J. Savary, D. Neuhauser, and S. Etchemendy, MOISE: A prototype multiparameter ocean-bottom station, *Bull. Seism. Soc. Am.*, 91, 885-892, 2001.

Uhrhammer, R., B. Romanowicz, D. Neuhauser, D. Stakes, P. McGill, and T. Ramirez, Instrument testing and first results from the MOBB Observatory, *EOS Trans. Amer. Geophys. Un.*, 83, F1008, 2002.

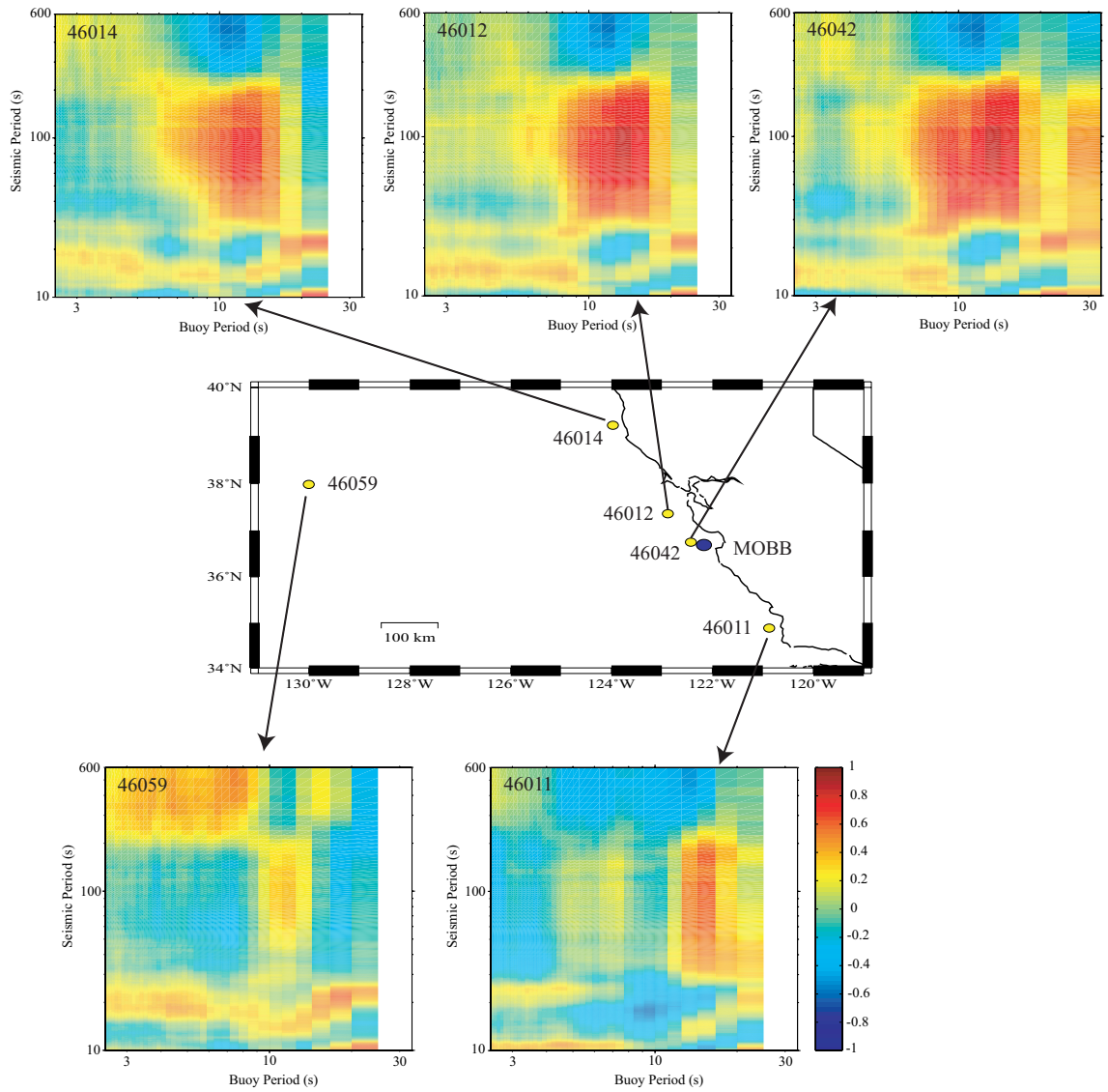


Figure 12.15: Correlations between power spectral density for the MOBB vertical channel and spectral wave densities measured on the closest buoys. Results for a 7-day period are shown. A color version of this figure is on page 103.

8. Slicing up the San Francisco Bay Area: Block Kinematics from GPS-derived Surface Velocities

Matthew A. d’Alessio, Ingrid A. Johanson, Roland Bürgmann, David A. Schmidt, and Mark H. Murray

The Berkeley Seismological Laboratory has collected and compiled interseismic velocities at over 200 Bay Area stations. This data set, the Bay Area Velocity Unification (BÄVÜ, pronounced “Bay View”) is the most comprehensive picture of crustal deformation in the region compiled to date. We use a block modeling approach to interpret these velocities at an unprecedented range of spatial scales. In this approach, we solve for the motion of fault bounded blocks that is most consistent with the observed surface velocities.

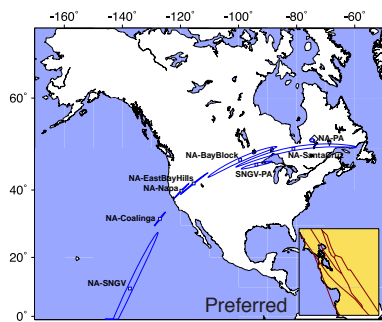


Figure 12.16: Calculated poles of rotation and 95% confidence limits for blocks in the Bay Area. Other than the Pacific-SNGV pole, all poles are relative to North America (NA). The diamond near Hudson Bay indicates the PA-NA from a two plate model that excludes stations near the plate boundary.

8.1 The Global Picture

Using the block model, we constrain the motion of blocks in the Bay Area relative to adjacent global plates (North America and Pacific), as well as the SNGV microplate. Individual blocks within the Bay Area do not move about identical poles of rotation of any of these major blocks as a “perfect transform” system, but instead have poles at intermediate locations. The poles transition systematically from west to east (Fig. 12.16). This systematic pattern may have implications for the development of the fault system.

8.2 Slip Rates on Bay Area Faults

We show a comparison between data and model velocities in (Fig. 12.17). Looking at the Bay Area region itself, we focus on quantifying the slip rates of individual

faults. We use precise relocations of earthquakes to determine the maximum depth of seismicity as a proxy for the local seismic/aseismic transition. We find slip rates that are typically within the uncertainty of geologic estimates (Table 12.1). We also document substantial slip on segments that have not been emphasized in previous studies. Models that include up to $4 \text{ mm} \cdot \text{yr}^{-1}$ of strike-slip on the West Napa fault north of San Pablo Bay provide almost identical model fit to those that exclude this fault. In our preferred model, we favor this geometry because it is consistent with geologic evidence showing that the some slip from the Calaveras fault is transferred westward, eventually connecting to the West Napa fault system. Adding a fault along the eastern margin of the Coast Range in our preferred model produces lower misfit and a geologically reasonable slip sense (right-lateral) on the Greenville – a notable improvement over models that exclude this “Valley Margin” deformation zone. This fault, running parallel to the San Andreas through central California carries $\sim 5 \text{ mm} \cdot \text{yr}^{-1}$ of right-lateral slip and $3 \text{ mm} \cdot \text{yr}^{-1}$ of fault-normal convergence. Poor data coverage near the model fault segment prevent us from determining if the deformation is accommodated by a single structure or a broad zone with many structures as might be implied by the distribution of moderate thrust earthquakes within the Diablo and Coast Ranges. We find that a similar magnitude of convergence is preferred along the entire eastern front of the Coast Range, but that an equal and opposite extension is observed west of the Bay in our models. Our block modeling approach provides the first strong geodetic constraints on the slip rates of several other faults because we include global GPS data from the Pacific plate and the physical constraint of coherent block motion. These faults include the San Gregorio fault ($2.4 \pm 0.5 \text{ mm} \cdot \text{yr}^{-1}$ right-lateral slip rate) and the Mount Diablo thrust ($3.9 \pm 0.5 \text{ mm} \cdot \text{yr}^{-1}$ reverse slip and an almost equal magnitude of right-lateral strike-slip). Overall, we find that the slip rates we determine fit GPS data substantially better than the slip rates defined in Working Group on California Earthquake Probabilities.

8.3 Fault Connectivity

Locally, block modeling allows us to test the connectivity of faults. Faults that are connected can transfer slip, so these connections have implications for slip rates and seismic hazard assessment. We show that shallow creep on Paicines fault is important, but that deep slip is best

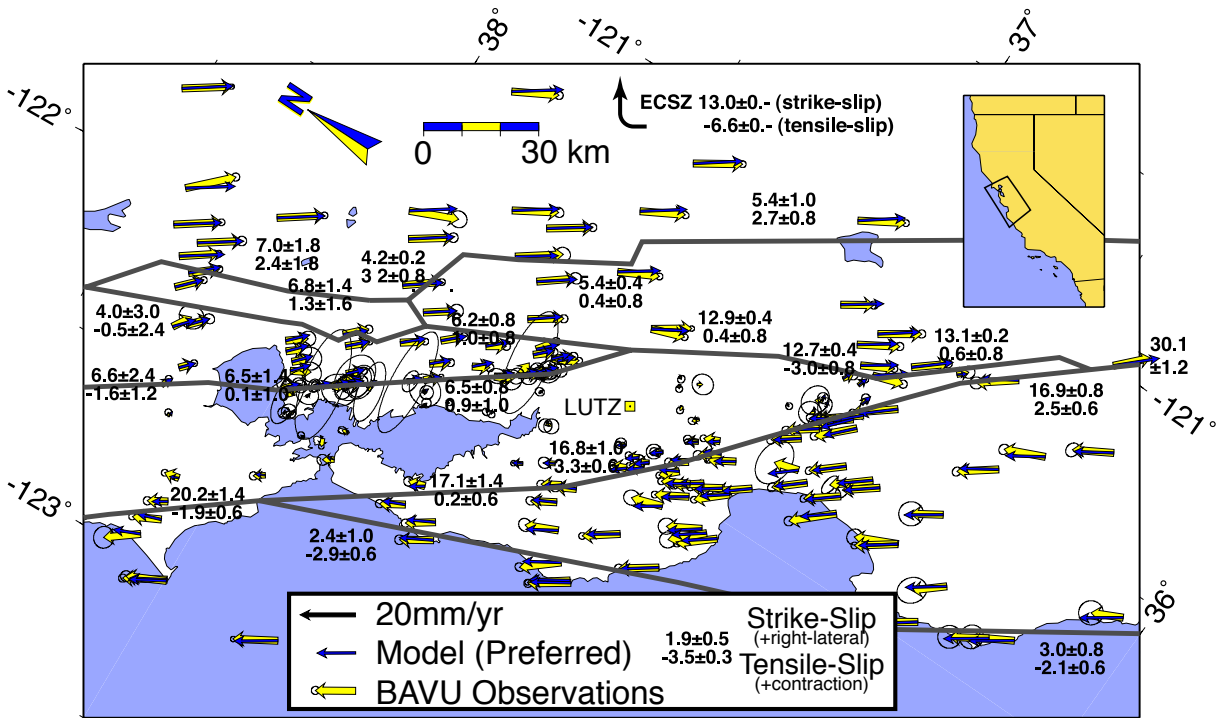


Figure 12.17: Observations (wider vectors with error ellipses) compared with model results (narrow, darker vectors) for our preferred model. Dotted grey lines represent the simplified geometry of faults in our model. Numbers indicate strike-slip and tensile-slip rates and 95% (2σ) uncertainties for select fault segments. Positive strike-slip indicates right-lateral slip. Positive tensile-slip indicates contraction while negative tensile-slip indicates extension.

modeled when the Calaveras fault is directly connected to both the Paicines and San Andreas faults. East of the Bay, we explore the possibility that the northern Calaveras fault transfers its slip east to the Concord/Green Valley fault, west to the West Napa fault system, or a combination of the two. The data slightly favor the eastern step over the western step alone, but we prefer models where both connections are included because they most closely reproduce the geologically inferred slip rate on the Green Valley fault and the lowest total model misfit.

In block modeling, three-dimensional fault geometry and connectivity have a very strong impact on the interpretation of surface deformation. While we systematically explored an extremely wide range of model geometries in this work, we look forward to further geologic constraints on fault geometry in 3-D to improve the reliability of block models. The ability to iteratively explore these different block geometries and test their consistency with geodetic data make the block modeling approach an excellent tool for understanding fault kinematics in the Bay Area.

Table 12.1: Comparison of strike-slip rates for geologic estimates (Working Group on California Earthquake Probabilities, WG03) and this study. Fault system names from top row: SG, San Gregorio; SA, San Andreas; RC, Rodgers Creek; H, Hayward; C, Calaveras; GV, Green Valley; Gr, Greenville. Fault segments from second row: N, North; C, Central; S, South; Mr, Marin; SF, San Francisco; SCM, Santa Cruz Mountains; RC, Rodgers Creek; H, Hayward; WN, West Napa; Cn, Concord; Gr, Greenville. Total for the northern section includes the sum of SA-Mrn + RC + WN + GV. Southern total is sum of SG-S + SA-SCM + C-C + Gr. We show 95% confidence bounds ($\pm 2\sigma$) for the three main models. Bounds for other models are similar in magnitude.

Study	SG		SA			RC/H		C			GV/Gr			Total		
	N	S	Mr	SF	SCM	RC	H	WN	N	C	S	GV	Cn	Gr	N	S
WG03	7	3	24	17	17	9	9	–	6	15	15	5	4	2	38	37
This Study	2.4	3.0	20.2	17.1	16.4	6.6	6.5	4.0	6.2	12.9	12.7	7.0	6.7	5.4	37.8	37.7
\pm	1.0	0.8	1.4	1.4	1.0	2.4	1.4	3.0	0.8	0.6	0.4	1.8	1.4	0.6	4.5	1.5

9. Active Tectonics of Northeast Asia: Using GPS Velocities and Block Modeling to Test Okhotsk Plate Motion Independent from North America

Edwin (Trey) Apel and Roland Bürgmann

9.1 Introduction

Horizontal surface velocities of 96 GPS sites (41 from the Eurasian, North American and Pacific plate and 55 from NE Asia) constrain the plate kinematics of NE Asia and allow for a rigorous test of the possibility of Okhotsk plate motion independent of the North American plate. A block modeling approach is used to incorporate both rigid block rotation and near-boundary elastic strain accumulation effects in a formal inversion of the GPS velocities. Considered models include scenarios with and without independent Okhotsk plate motion and a number of different plate boundary locations and locking depths. We are also considering the possible influence of an independent Amurian plate that may also affect the determination of Okhotsk plate existence and motion.

9.2 Background

The current plate kinematics of Northeast Asia are somewhat enigmatic due to subduction dominated deformation in the east and little to no differential plate motion in the west which results in diffuse and sparse seismicity. An Okhotsk plate that rotates independently of North America is not a particularly new idea (*Seno et al.*, 1996). However, it is important for defining the plate boundary geometry and constraining the relative motion of the major and minor plate in Northeast Asia and provides a rigorous framework for interpreting seismicity and the surface deformation observed by geodesy. Because the increasingly dense GPS networks in this region are in such close proximity to plate boundaries a sophisticated plate motion model that includes both rigid block rotations and elastic plate boundary strain effects is required to discriminate independent Okhotsk plate motion.

9.3 GPS Velocities

The GPS velocities used in our inversion are an updated subset of the 151 global stations processed for the final solution by *Steblov et al.* (2003). The data were processed using GAMIT/GLOBK by Bob King at MIT and Misha Kogan at Columbia. Processing details can be found in *Steblov et al.* (2003). Before our inversion the GPS sites were weighted according to site stability, distance from plate boundaries, and a simple declustering routine.

9.4 Blocks

In order to test for independent Okhotsk plate motion we tested two block configurations. In our 3-plate system we assumed that the Okhotsk region was part of the North American plate (Figure 12.18). Our 4-plate model (Figure 12.19) allows the Okhotsk plate to rotate independently. We then compared the misfit of the inversion to the data to test for significance. The segments that bound the blocks represent uniformly slipping elastic dislocations locked to some specified depth. Because our inversion combined rigid block rotation with elastic strain accumulation effects, the parameterization of the block boundary geometry is critical. Geometry of the plate boundaries was based heavily on seismicity. However, topography, geodetic gradients, and other modeling (such as single distributed slip inversions) were used to constrain the location and strike and dip of some of our elastic dislocations. Diffuse boundaries surrounding the Okhotsk region like the northern and western edges are not manifested as discrete structures in any geological or geophysical data set. These plate boundary deformation zones are represented in our model by vertical dislocations locked to optimal depths of approximately 75 km that are allowed both strike-slip and tensile motions. These deeply locked elastic dislocations generate diffuse surface deformation consistent with observed patterns of surface deformation. The kinematics of subduction zones are represented by dipping dislocations, locked to 40 km depth and allowed to accommodate both strike slip and dip slip motion.

9.5 Inversion

The GPS data and pre-defined block boundary geometry were used as inputs in our block modeling inversion code (*Meade and Hager*, 2004). We used all of these data (96 sites) to invert for predicted horizontal surface velocities at each GPS station while simultaneously considering rigid block rotation and elastic strain effects for both block configurations. Our 3-plate model shows a clear, systematic pattern of residual velocities that suggests independent Okhotsk plate motion (Figure 12.18). Euler vectors, calculated from our optimized 4-plate inversion, suggest the Okhotsk plate rotates 0.206 deg/Myr clockwise, with respect to North America, about a pole located north of Sakhalin (Figure 12.19 inset).

9.6 Discussion and Conclusions

Our inversion favors a scenario with independent Okhotsk plate motion but does not require it, based on the application of F-test statistics, which indicate that the improved fit is significant only at 87% confidence. The plate-motion parameters of the Okhotsk plate are consistent with right-lateral motion in northern Sakhalin and contraction in southern Sakhalin, inferred from focal mechanism solutions. However, subtle changes in block and segment geometry can cause significant changes in the estimated pole of rotation of the Okhotsk plate. This is due, in large part, to the close proximity of most GPS stations in northeast Asia to plate boundaries, such as the Kamchatka-Kurile subduction zone and the Sakhalin Island contraction and strike-slip shear zone. GPS velocities on the Kamchatka peninsula capture a complex pattern associated with the locked subduction zone. This locked subduction zone may require a more complex model than a simple elastic dislocation for the rotational signal to be resolvable. Additional blocks may also affect the determination of an independently rotating Okhotsk plate. Our continued work includes formally examining the potential role of adjacent blocks such as the Amurian, northern Hokkaido, and Magadan blocks.

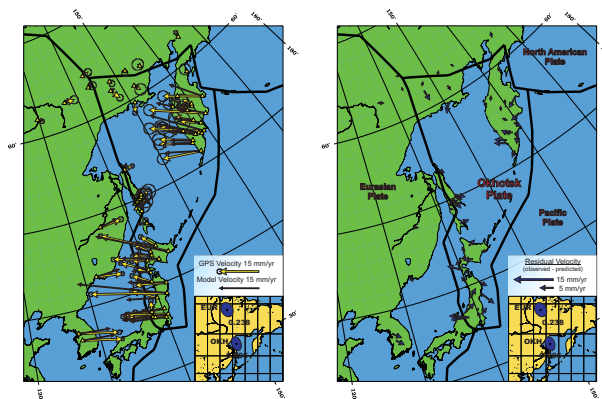


Figure 12.19: Observed, predicted, and residual velocities for the 4-plate model. The inset map shows the position of the Eurasian and Okhotsk poles of rotation (2-sigma error ellipses) with respect to North America and are labeled in degrees per million years.

American plate in Siberia revealed by GPS, *Geo. Res. Let.*, **30(18)**, 2003.

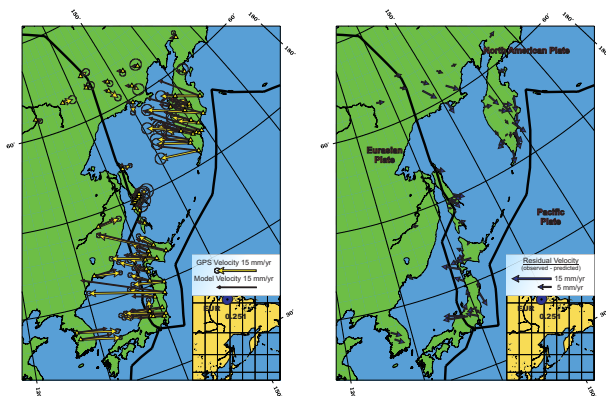


Figure 12.18: Observed, predicted, and residual velocities for the 3-plate model. The inset map shows the position of the Eurasian pole of rotation (2-sigma error ellipses) with respect to North America and is labeled in degrees per million years.

9.7 References

Meade, B.J. and B.H. Hager, Block Models of Crustal Motion in Southern California Constrained by GPS Measurements, *J. Geophys. Res.* (**IN PRESS**), 2004.

Seno, T., T. Sakurai, and S. Stein, Can the Okhotsk plate be discriminated from the North American plate?, *J. Geophys. Res.*, **101**, 11305-11315, 1996.

Steblov, G.M., M.G. Kogan, R.W. King, C.H. Scholz, R. Bürgmann, and D.I. Frolov, Imprint of the North

10. The Spatial Pattern of Active Uplift in Eastern Taiwan

Leslie Hsu and Roland Bürgmann

10.1 Introduction

The eastern coast of Taiwan is one of the most actively deforming regions in the world, with present-day convergence at 8 cm/year where the Luzon Arc is colliding with the Eurasian Plate (Yu *et al.*, 1997). The Eastern Coastal Range is thrust upwards along the east-dipping Longitudinal Valley Fault (LVF), accommodating about 3 cm/yr of the convergence (Yu *et al.*, 1997). Present-day active uplift along the fault is constrained by a GPS network and leveling measurements, showing along-strike variation in rates of slip (Yu and Kuo, 2001). In addition, the marine terrace record indicates that some segments of the LVF have been uplifting more rapidly than others over the timescale of the Holocene (Hsieh *et al.*, 2004). We are using InSAR to improve our knowledge of present-day vertical movement and strain accumulation along the Longitudinal Valley Fault.

The new InSAR data, yielding an improved velocity field, will be used to both reevaluate previous dislocation models and formulate new models. These improvements may help to explore currently unresolved issues such as the location of strain accommodation near in the northern half of the LVF within the Coastal Range or on proposed offshore faults (Bos *et al.*, 2003; Yamaguchi and Ota, 2004). We will also investigate the uplift patterns perpendicular and parallel to the faults strike. The former will tell us to what extent the Coastal Range is uplifting like a rigid block and the latter will illustrate transitions between locked and creeping sections of the fault.

10.2 Results

From 9 SAR scenes, we created 13 unwrapped interferograms from pairs spanning one month to 2.5 years. We made three stacks of 3-4 interferograms in an attempt to average out atmospheric effects. In some stacks, the recent mapped fault trace correlates well with an offset in the phase signal. Near Chishang, we measured a maximum offset across the fault that gave 14-26 mm/yr movements in the slip direction (Figure 12.20), agreeing well with the nearby creepmeter data (Lee *et al.*, 2003). However, this signal is not present everywhere along the fault.

We are developing an interseismic model that will be used as the basis for estimating and removing an orbital ramp from each interferogram. The interseismic model is produced from a simple fault geometry in an elastic half-space. We have also compiled horizontal and vertical GPS measurements, creepmeter data, leveling data, and current fault traces for comparison with the interfer-

ometry. Combining these different measures of deformation, we hope to achieve a better understanding of the nature and origin of spatial variation of movement along the Longitudinal Valley Fault.

10.3 Acknowledgements

This research is made possible by the Francis Turner Fellowship and a University Fellowship granted by the Taiwanese-American Foundation of Boston.

10.4 References

Bos, A.G., W. Spakman, and M.C.J. Nyst, Surface deformation and tectonic setting of Taiwan inferred from a GPS velocity field, *J. Geophys. Res.*, 108(B10), 2458, doi:10.1029/2002JB002336, 2003.

Hsieh, M.L., P.M. Liew, and M.Y. Hsu, Holocene tectonic uplift on the Hua-tung coast, eastern Taiwan, *Quatern. Int.*, 115, 47-70, 2004.

Lee, J.C., J. Angelier, H.T. Chu, J.C. Hu, F.S. Jeng, and R.J. Rau, Active fault creep variations at Chihshang, Taiwan, revealed by creep meter monitoring, 1998-2001, *J. Geophys. Res.*, 108(B11), 2528, doi:10.1029/2003JB002394, 2004.

Yamaguchi, M., and Y. Ota, Tectonic implications of Holocene marine terraces, east coast of Coastal Range, Taiwan, *Quatern. Int.*, 115, 71-81, 2004.

Yu, S.B., H.T. Chen, and L.C. Kuo, L.C., Velocity field of GPS stations in the Taiwan area, *Tectonophysics*, 274, 41-59, 1997.

Yu, S.B., and L.C. Kuo, Present-day crustal motion along the Longitudinal Valley Fault, eastern Taiwan, *Tectonophysics*, 333, 199-217, 2001.

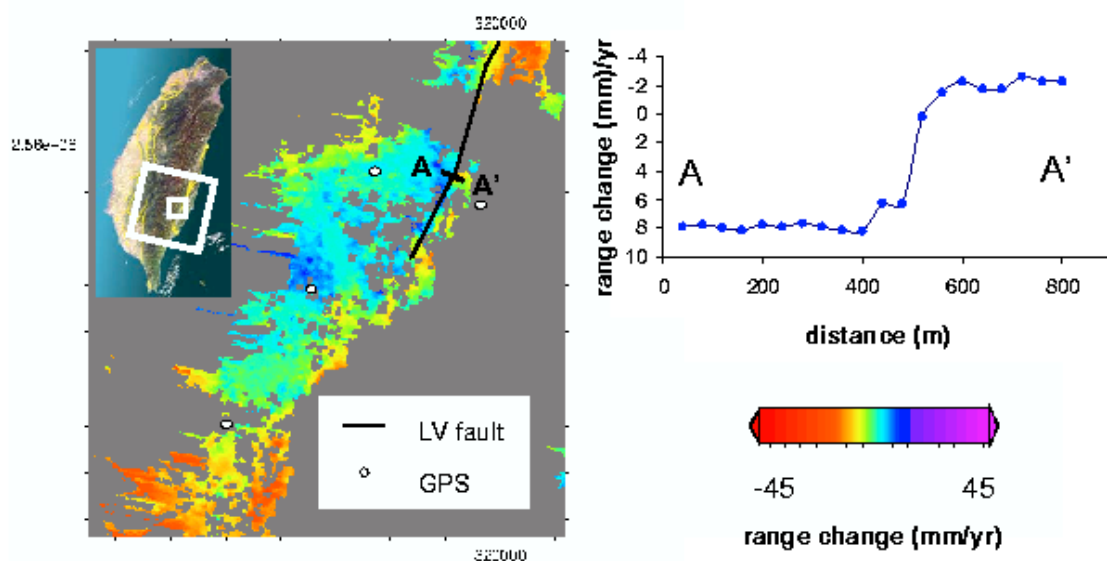


Figure 12.20: Location map, unwrapped interferometry, and offset on the Longitudinal Valley Fault, near Chishang. The interferogram is produced from a stack of three pairs spanning 1997 to 2000 (970517-980502, 970726-980815, 980815-000122). We calculated 14-26 mm/yr offset in the slip direction across the fault from A to A'.

11. Crustal Deformation Along the Northern San Andreas Fault System

Mark H. Murray

11.1 Introduction

The San Andreas fault system in northern California includes three sub-parallel right-lateral faults: the San Andreas, Ma'acama, and Bartlett Springs. This northernmost segment is the youngest portion of the fault system, forming in the wake of the northwestwardly propagating Mendocino triple junction where the Pacific, North America, and Gorda (southern Juan de Fuca) plates meet. The Pacific plate moves about 35-40 mm/yr relative to central California across a broad ~100-km zone in northern California. Additional deformation in eastern California and the Basin and Range province contribute to the total relative Pacific-North America motion of ~50 mm/yr. The San Andreas fault itself has been essentially aseismic and accumulating strain since it last ruptured in the great 1906 San Francisco earthquake, and no major earthquakes have occurred during the historical record on the more seismically active Ma'acama, and Bartlett Springs faults, which are northern extensions of the Hayward-Rodgers Creek and Calaveras-Concord-Green Valley faults in the San Francisco Bay area.

In *Frey Mueller et al.* (1999), we used GPS data collected in 1991-1995 along two fault-crossing profiles near Ukiah and Willits (Figure 12.21). The total deep slip rate on the San Andreas fault system inferred from the GPS data is $39.6^{+1.5}_{-0.6}$ mm/yr (68.6% confidence interval). Although deep slip rates on the individual faults are more poorly resolved due to high correlations between estimated slip rates and locking depths, and between slip rates on adjacent faults, the inferred slip rate on the Ma'acama fault ($13.9^{+4.1}_{-2.8}$ mm/yr) implies that it has accumulated a slip deficit large enough to generate a magnitude 7 earthquake, posing a significant seismic hazard.

In this ongoing study, we are resurveying the original profiles, adding new profiles to the north (near Covelo) and south (near Healdsburg), and surveying nearly 40 additional stations in the southern portion of the network to provide better monitoring along the Rodgers Creek and Ma'acama faults (Figure 12.21). The survey of the 4 primary profiles was conducted during 2003. Altogether, 43 site positions were measured during 94 session occupations lasting 6.5-8 hours, with the assistance of students and staff of the BSL. We are currently surveying about 40 monuments in the southern portion of network and are planning to install new profiles in special focus areas along the Bartlett Springs fault, whose long-term slip rate, locking depth and surface creep are poorly resolved. Most of the monuments were last observed in 1993-1995,

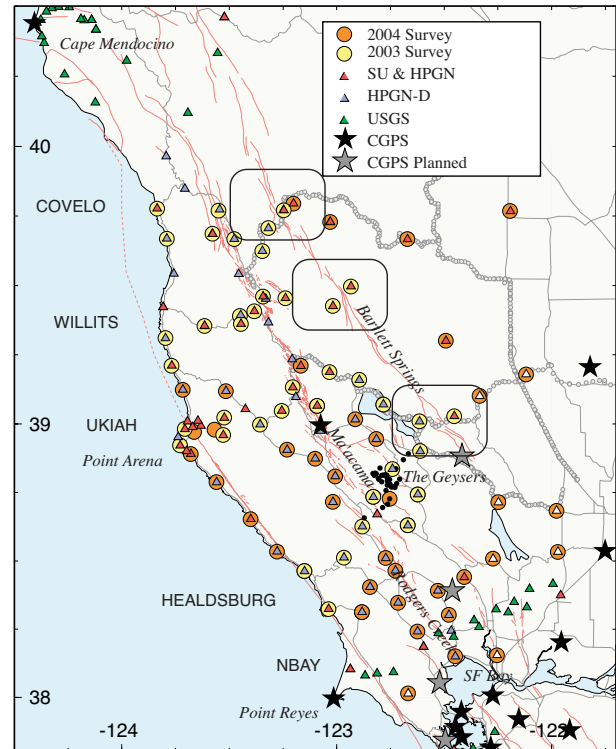


Figure 12.21: GPS sites along the northern San Andreas fault system. Light circles, sites that were observed in early 2003. Dark circles, 2004 surveyed or planned stations. Profile names are capitalized. USGS conduct surveys along the NBAY profile and near Cape Mendocino. Only one continuous GPS station (HOPB) currently operates in this region, with at least 5 planned PBO stations to be installed in Summer and Fall 2004. Rounded boxes, special focus areas along the Bartlett Springs fault where we will establish new profiles in Fall 2004.

so the new observations significantly improve the velocity estimates and models of average interseismic strain accumulation, including possible spatial variations along the fault system. The 10-station profiles from Pt. Reyes to Cape Mendocino together with planned PBO stations form a primary monitoring network for future observations to detect temporal variations in deformation.

11.2 Deformation

Figure 12.22 shows site velocities for the 1994-2004 period relative to stable North America, as defined by a set of 20 fiducial stations. The data are processed using

GAMIT/GLOBK software using many of the same techniques used to process the BARD observations described in Chapter 6 that provide a well-defined velocity reference frame with respect to the stable North America. Most of the velocities were derived from data spanning 8-10 years, whereas those with the largest error ellipses include data from only a 4 year span (most of these stations will be reoccupied in 2004). The easternmost stations exhibit motions typically associated with Sierran-Great Valley block (ORLA: 12.5 mm/yr NW). The westernmost sites are moving close to the Pacific plate rate (PTAR: 45.9 mm/yr NW). Fault-normal contraction is observed east of the Ma'acama fault, in the region of the Coast Ranges near the Central Valley where similar contraction has been observed elsewhere (e.g., *Murray and Segall, 2001*).

We apply angular velocity-fault backslip modeling techniques (e.g., *Murray and Segall, 2001*) to account for both far-field plate motions and interseismic strain accumulation. We are currently using a set of algorithms provided by Brendan Meade of MIT that extend this simple 2D methods to complex, 3D fault systems (including subduction zones and extensional provinces) by summing backslip on rectangular dislocations. We have successfully used the algorithms in a study of block motions in the Adriatic region and in the the BAVU block modeling efforts for the San Francisco Bay Area, both of which are described in other research chapters.

Preliminary results from our block modeling efforts are shown in Figure 12.22. We assume a simple fault geometry with 2 blocks between the 3 major faults in the San Andreas fault system. We also include the Pacific and North America plates, with sufficient numbers of stations to resolve their relative motions, and a Sierran-Great Valley block to provide better constraints on motions just east of the Bartlett Springs fault. The agreement between observed and predicted velocities is typically less than the 2 mm/yr level. Misfits are larger in a few areas close to faults, such as along the central Ma'acama and near the MTJ, that should be decreased with further refinement of the fault geometry. Total deformation across the San Andreas fault system is 38 mm/yr, in agreement with previous studies, but deep slip is concentrated on the Ma'acama fault (24 mm/yr) and on the Bartlett Springs fault (10 mm/yr), with only 4 mm/yr on the San Andreas. We are currently investigating this result, which is due in part to the high-degree of correlation between the slip rates on the 3 faults, and will test methods for adding geologic and other information using Bayesian techniques, which should reduce the correlations on slip rates and provide better resolution on other parameters such as locking depths. Fault normal contraction of about 3 mm/yr is estimated due to the impingement of the Sierran-Great Valley on the fault system, but more sophisticated error analysis is required to

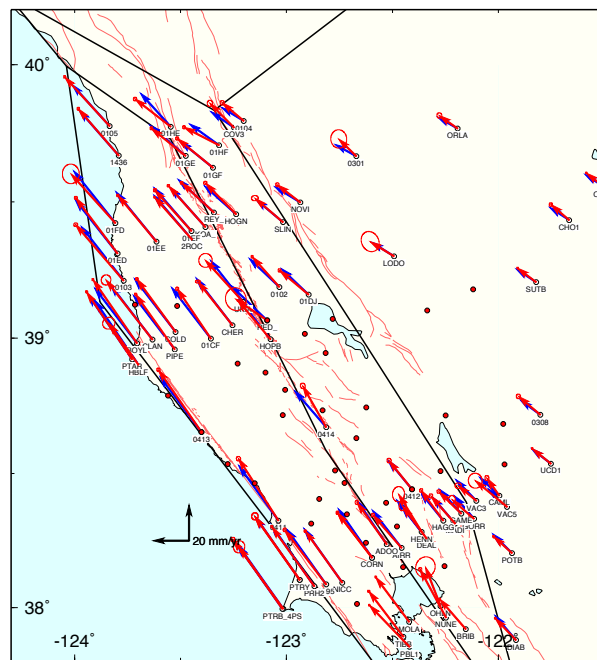


Figure 12.22: Velocities of sites in the Coast Ranges relative to North America, with 95% confidence regions assuming white-noise process only. Included are sites from this study plus sites from the BARD continuous network and the USGS North Bay profile. Red, observed velocities. Blue, velocities predicted from angular velocity-backslip block model assuming block boundaries (heavy black lines). We assume Pacific, North America, and Sierran-Great Valley blocks, plus 2 small blocks between the San Andreas, Ma'acama, and Bartlett Springs faults. The most significant misfits, such as near Cape Mendocino, can be reduced by refining the fault geometry.

assess whether this result is significant.

11.3 Acknowledgements

We appreciate support for this project by the USGS NEHRP through grant numbers 02HQGR0064 and 03HQGR0074. We thank André Basset, Maurizio Battaglia, Dennise Templeton, and especially Todd Williams for assistance conducting the survey.

11.4 References

- Frey Mueller, J. T., M. H. Murray, P. Segall, and D. Castillo, Kinematics of the Pacific-North America plate boundary zone, northern California, *J. Geophys. Res.*, 104, 7419–7442, 1999.
- Murray, M. H., and P. Segall, Modeling broadscale deformation in northern California and Nevada from plate motions and elastic strain accumulation, *Geophys. Res. Lett.*, 28, 4315–4318, 2001.

12. The Adriatic Region: An Independent Microplate within the Africa-Eurasia Collision Zone

Maurizio Battaglia, Mark H. Murray, Enrico Serpelloni (INGV) and Roland Bürgmann

12.1 Introduction

The tectonics of the Mediterranean is shaped by deformation related to the collision between the Nubia (Africa), Eurasia, and Anatolia plates. In this study, we use block modeling of surface velocities recorded by GPS measurements (Battaglia *et al.*, 2004) to investigate the present-day deformation of the Adriatic (Figure 12.23).

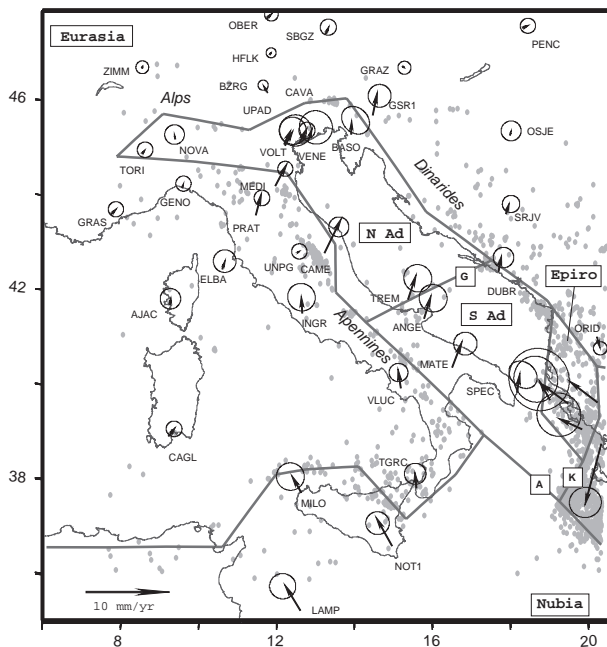


Figure 12.23: Location of the segments (solid lines) and blocks used to model the Adriatic region. [N Ad] North Adria, [S Ad] South Adria. [G] Gargano-Dubrovnik fault zone; [K] Kefallinia fault zone; [A] Apulia escarpment. GPS velocities and their 95% confidence ellipses. The grey dots indicate the location of the shallow seismicity from 1975 to 2000 ($M > 3.5$).

The tectonics of the Adriatic is not well constrained and remains controversial. Given the lack of significant seismic activity along the southern margin of the Adriatic Sea, the boundary with the Nubia plate, if it exists, is not well defined. Geomagnetic data averaged over several Myr and S_n shear wave propagation observations suggest that Nubia extends as a promontory into the Adriatic region (Mele, 2001), whereas historic geodetic and seismic evidence suggest that the Adriatic is an independent microplate (Adria) within the Nubia-Eurasia plate bound-

ary zone (Nocquet and Calais, 2003). Oldow *et al.* (2002) propose that Adria is divided by the Gargano-Dubrovnik fault into two blocks. Northwestern Adria has little or no motion relative to Europe and is part of the Alpine collage of southern Europe. Southeastern Adria is moving together with Nubia and is continuous from Sicily to Apulia. Other studies suggest that the Adriatic is an area of distributed deformation (Nocquet *et al.*, 2001).

To test different tectonic models for the Adriatic region, we develop a block model of regional deformation (Figure 12.23). This approach incorporates secular velocity and fault geometry estimates, as well as elastic strain accumulation. With this model we can assess whether different hypotheses are compatible with geodetic data, estimates of fault slip rates and locking depths, areas of rigid block rotation, and regions of anomalous strain accumulation (Meade *et al.*, 2002; Battaglia *et al.*, 2004).

12.2 GPS Measurements of Deformation

We use publicly available observations made at 30 continuous GPS stations of the European Reference Permanent Network (EUREF) and Italian Space Agency networks to estimate deformation in the Adriatic region (Figure 12.23). To improve the realization of a stable reference frame for the velocity solution, additional sites from the International GPS Service and EUREF networks are included as loosely constrained solutions provided by the Scripps Orbit and Permanent Array Center. Our solution includes data spanning 4 years from 102 stations, including 50 in the Mediterranean area. We incorporate velocities from 38 episodic GPS (EGPS) sites from McClusky *et al.* (2000) and 10 EGSP sites from Serpelloni *et al.* (2001) to better constrain deformation in the Eastern Mediterranean (Aegean and Anatolian plates) and southern Adriatic regions.

12.3 Block Model

Our block model of the Adriatic includes the interaction between the Eurasia, Nubia, Adria, Anatolia, Aegea, and Arabia plates. The plate boundaries are based on the description of the tectonic settings of the Mediterranean after van Dijk and Scheepers (1995), and seismicity distribution in the in the Mediterranean basin (International Seismological Center, 2001).

Plate boundary strain is determined from single continuous faults along the Calabrian coast, the Apennines, the Alps, the Dinarides, and the Hellenic Arc (Figure 12.23). This approach provides a first-order kinematic

description in areas with more broadly distributed deformation, where the station distribution is insufficient for detailed study.

We evaluate several possible representations of Adria and the Adria-Nubia margin: (1) the Adriatic is a region of continuous deformation within the Eurasian plate; (2) Northwestern Adria is part of the Alpine collage of southern Europe with the southern boundary with Nubia being the Gargano-Dubrovnik fault; (3) Nubia extends as a promontory into the Adriatic region; (4) Adria is divided from Nubia by the Gargano-Dubrovnik fault; (5) Adria is divided from Nubia and Aegea by the Apulia Escarpment and the Kefallinia fault; (6) Adria consists of two blocks separated by the Gargano-Dubrovnik fault in the middle and divided from Nubia and Aegea by the Apulia Escarpment and the Kefallinia fault.

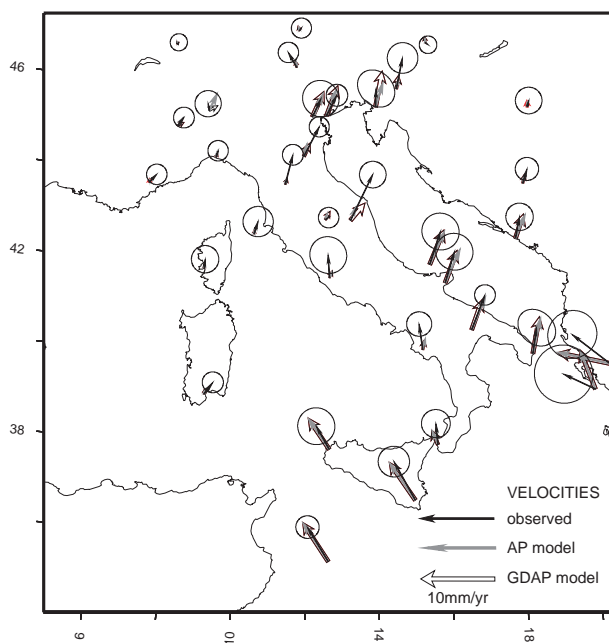


Figure 12.24: Observed and modeled GPS velocities for the single block (AP) and the two blocks (GDAP) model of Adria.

12.4 Results

The geodetic data and the models presented here (Figure 12.24) indicate that the Adriatic block is neither part of the Eurasia nor the Nubia plate. Geodetic data show that the Nubia plate is moving NW with respect to Eurasia with a velocity of 6 mm/yr, while the Adriatic microplate moves NE at a rate of 4-5 mm/yr (McClusky *et al.*, 2000). Our results show that independent microplate models of Adria offer a better fit to GPS velocities than models considering Adria as continuous with the Nubia or Eurasia plate. Geodetic data alone can-

not discriminate between a single block (AP) or a two block (GDAP) description of Adria (Figure 12.24), but the GDAP model predicts boundary slip rates that are in better agreement with observations from previous studies. Modeling results suggest that a possible location of the southern Adriatic/Nubia boundary could be the Apulia Escarpment lineament.

12.5 Acknowledgements

We acknowledge the GEODAF data archive of the Italian Space Agency (ASI) for providing GPS data. B. Meade (MIT) kindly allowed the use of his block model code. This work was supported by the Berkeley Seismological Laboratory and the Istituto Nazionale di Oceanografia e Geofisica Sperimentale (CRS-INOGS).

12.6 References

- Battaglia M., Murray M.H., Serpelloni E., and R. Bürgmann. The Adriatic region: an independent microplate within the Africa-Eurasia collision zone. *Geophys. Res. Lett.*, 31(9), L09605, 10.1029/2004GL019723, 2004.
- McClusky, S., et al., Global Positioning System constraints on plate kinematics and dynamics in the eastern Mediterranean and Caucasus, *J. Geophys. Res.*, 105, 5695-5719, 2000.
- Meade, B.J. et al., Estimates of seismic potential in the Marmara Sea region from block models of secular deformation constrained by Global Positioning System measurements, *Bull. Seism. Soc. Am.*, 92, 208-215, 2002.
- Mele, G., The Adriatic lithosphere is a promontory of the Africa Plate; evidence of a continuous mantle lid in the Ionian Sea from efficient S_n propagation, *Geophys. Res. Lett.*, 28, 431-434, 2001.
- Nocquet, J.M., and E. Calais, Crustal velocity field of Western Europe from permanent GPS array solutions, 1996-2001, *Geophys. J. Int.*, 154, 72-88, 2003.
- Nocquet, J.M., E. Calais, Z. Altamini, P. Sillard, and C. Boucher, Intraplate deformation in Western Europe deduced from an analysis of the International Terrestrial Reference Frame 1997 (ITRF97) velocity field, *J. Geophys. Res.*, 106, 11,239-11,257, 2001.
- Oldow, J.S. et al., Active fragmentation of Adria, the north Africa promontory, central Mediterranean orogen, *Geology*, 30; 779-782, 2002.
- Serpelloni, E., et al., Combination of permanent and non-permanent GPS networks for the evaluation of the strain-rate field in the central Mediterranean area. *Boll. Geof. Teor. Appl.*, 43, 195-219, 2002.
- van Dijk, J.P., and P.J.J. Scheepers, Neotectonic rotations in the Calabrian Arc; implications for a Pliocene-Recent geodynamic scenario for the Central Mediterranean, *Earth-Science Rev.*, 39, 207-246, 1995.

13. Bayesian Inference of Lower-Crustal Viscosity Near the Kunlun Fault Based on Geologic, Geomorphic, and Geodetic Data

George E. Hilley, Roland Bürgmann, Pei-Zhen Zhang (State Key Laboratory of Earthquake Dynamics, Beijing, China), and Peter Molnar (University of Colorado, Boulder, USA)

13.1 Introduction

Bayesian methods provide the means of integrating geologic, paleoseismic, seismic, and geodetic data to improve estimates of fault zone and lower-crustal properties (e.g., Segall, 2002) that are important for predicting the long-term deformation of plate boundary zones (e.g., Shen et al., 2001), understanding deformation and stress transfer following earthquakes, and estimating future seismic hazard (e.g., Hardebeck, 2004). Herein, we develop a Bayesian methodology that integrates geologic, geomorphic, and geodetic data to provide probabilistic estimates of fault-zone and lower-crustal properties.

We will apply this methodology to the Kunlun Fault in northern Tibet (Figure 12.25), where estimates of lower-crustal viscosity are generally lacking. Here, geologic and geomorphic information constrain the range of permissible long-term slip rates and coseismically generated offsets. We combined these a priori estimates with GPS velocities using a Bayesian implementation of an elastic-viscoelastic earthquake cycle model (Savage and Prescott, 1978) to estimate fault-zone and lower crustal properties in the area. The probabilistic nature of these models allows straightforward assessments of the uncertainties within, and covariance between model parameters. Our example shows that these methods may aid in elucidating the active tectonics of other areas, and improve seismic hazard assessments by formally assimilating disparate data types (e.g., geologic, geomorphic, seismic, or geodetic datasets) into crustal deformation studies.

13.2 Bayesian Modeling Framework

The Bayesian approach that we use to analyze data from northern Tibet uses geologic and geomorphic estimates of fault slip rates and observed offsets in conjunction with geodetic data to refine estimates of fault slip rate, schizosphere thickness, recurrence time of events, and viscous relaxation time of the plastosphere (“chizosphere” refers to the portion of the upper crust that deforms elastically, while “plastosphere” refers to areas that deform elastically over short time-scales but undergo viscous stress relaxation over longer time-scales; Scholz, 1988). Our method is based on Bayes’ Rule (Bayes, 1763), which allows quantitative refinement of initial estimates of model parameters (in this case, fault zone and lower crustal properties) given the information provided by the geodetic observations (Segall, 2002; Johnson and Segall, 2004):

$$P(m_i|x) = \frac{P(x|m_i) \times P(m_i)}{\sum_{i=1}^n P(x|m_i) \times P(m_i)} \quad (12.1)$$

In the context of this paper, m_i denotes a vector of model parameters, x is a vector of the observed geodetic velocities, $P(m_i|x)$ denotes the probability that the set of model parameters explains the geodetic velocities, $P(x|m_i)$ is the probability of observing the geodetic velocities given a combination of model parameters m_i , $P(m_i)$ is the probability that the chosen combination of model parameters actually occur, and the denominator normalizes the probability to all possible combinations of model parameters. In this context, $P(x|m_i)$ encapsulates the goodness of fit between observed geodetic velocities and those that would be expected based on the physical model that relates the surface velocity distribution to fault-zone and lower crustal properties (described below). Geodetic inversions that find the set of model parameters that best explain the observed data maximize $P(x|m_i)$. In contrast, the Bayesian approach not only considers the goodness of fit of the velocity to model predictions, but also $P(m_i)$, which describes in a probabilistic sense, some prior knowledge about what sets of model parameters are likely to occur. This term may be used to incorporate information such as slip rates along faults and recurrence times of earthquakes whose range may be estimated based on geologic and geomorphic considerations (e.g., Buck et al., 1996; Biasi et al., 2002; Segall, 2002). Therefore, the Bayesian modeling strategy has a two-fold advantage to conventional geodetic inversions: 1) Uncertainties in model parameters and covariance between model parameters may be straightforwardly obtained for complicated models (e.g., Hargreaves and Annan, 2002); and 2) Other types of data (e.g., geologic, geomorphic, and paleoseismic) may be used in conjunction with the geodetic data to improve estimates of model parameters. Explicit evaluation of Equation 12.1 may be untenable for potentially large, multidimensional parameter spaces that may arise even in simple physical models such as the model described below. Therefore, we solve Equation 1 using the Metropolis-Hastings variant of the Markov-Chain Monte Carlo (MCMC) simulation methods that allows approximation of the joint distribution $P(m_i|x)$ without an exhaustive search of the parameter space (Metropolis et al., 1953).

The mechanical model we employ (evaluated through $P(x|m_i)$) idealizes earthquake-cycle deformation as resulting from elastic strain release during rupturing events

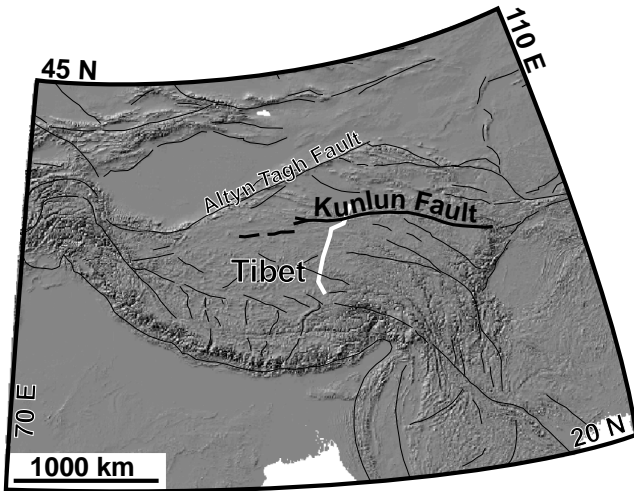


Figure 12.25: Location of the Kunlun Fault in central Asia. The Kunlun fault is one of a series of strike-slip faults that may accommodate a portion of the Indo-Eurasian collision. White line shows approximate location of GPS profile used in this study.

followed by viscoelastic relaxation of the lower crust and upper mantle (e.g., Savage and Prescott, 1978). The crust is idealized as two-dimensional in cross-section, and so movement along the major strike-slip faults occurs in the out-of-plane dimension. The rheology of the crust is treated as a two-layered medium in which an elastically deforming schizosphere overlies a linear, visco-elastically deforming plastosphere (e.g., Savage and Prescott, 1978; Savage, 2000; Segall, 2002; Dixon et al., 2003). The deformation during the earthquake cycle is defined by the long-term, average strike-slip velocity of the modeled fault (s), the Maxwell relaxation time of the plastosphere ($\tau = 2\nu/\mu$, where ν is the viscosity and μ is the shear modulus), the thickness of the schizosphere (H), the time since the last earthquake (t), and the average recurrence interval (T). Following Savage and Prescott (1978) and Segall (2002), we non-dimensionalize the model by introducing four groups: $t^* = t/T$, $\tau^* = \tau/T$, $s^* = s/s_{ref}$, and $H^* = H/x_{ref}$, where s_{ref} and x_{ref} are arbitrary velocity and length scales set to 1 mm/yr and 1 km, respectively. Although this is a simple representation of the earthquake cycle, this model is appropriate for inferring slip rates along the Kunlun Fault (and active strike-slip faults in Tibet in general) because: 1) The model captures the basic observation that the crustal deformation during the seismic cycle consists of coseismic, elastic, deformation followed by postseismic viscoelastic adjustment of the lower crust (e.g., Savage and Prescott, 1978; Segall, 2002); and 2) Several previous studies have successfully employed these types of simple models to provide first-order estimates of fault zone and lower-crustal

properties. Given the density of geodetic measurements from this portion of Tibet, the earthquake cycle modeling we employ allows us to consider velocity variations during the earthquake cycle that cannot be assessed using the types of dislocation models currently employed to interpret interseismic geodetic velocities from this area (i.e., Wallace et al., 2004; Zhang et al., 2004).

13.3 Application to the Kunlun Fault

Along the Kunlun Fault, numerous studies show consistency in estimated slip rates over a variety of different time-scales (10-100 kyr time-scales), and so the primary goal of the specific example is to estimate lower-crustal properties beneath the Kunlun fault based on geologic, geomorphic, and geodetic datasets. Along the Kunlun fault, 1) Geologic and geomorphic studies indicate that long-term slip rates are between 9-16 mm/yr (Kidd and Molnar, 1988; van der Woerd et al., 2001); 2) Geomorphic studies and historic ruptures suggest that the slip during each event is approximately 10 m (van der Woerd et al., 2001); and 3) The lack of historic seismicity places a minimum bound on the recurrence time of earthquakes along the fault. Using this information, we will construct prior joint probability densities and apply our Bayesian methodology to refine estimates of each of these parameters and the Maxwell relaxation time of the lower crust.

13.4 References

- Bayes, T., An essay towards solving a problem in the doctrine of chances, *Phil. Trans. R. Soc. Lond.*, 53, 370-418, 1763.
- Biasi, G. P., R. J. Weldon II, T. E. Fumal, and G. G. Seitz, Paleoseismic event dating and the conditional probability of large earthquakes on the southern San Andreas Fault, California, *Bull. Seism. Soc. Am.*, 92, 2761-2781, 2002.
- Buck, C. E., W. G. Cavanagh, and C. D. Litton, *The Bayesian Approach to Interpreting Archaeological Data*, Wiley, Chichester, 382 pp, 1996.
- Dixon, T. H., E. Norabuena, and L. Hotaling, Paleoseismology and Global Positioning System: Earthquake-cycle effects and geodetic versus geologic fault slip rates in the Eastern California shear zone, *Geology*, 31, 55-58, 2003.
- Hardebeck, J. L., Stress triggering and earthquake probability estimates, *J. Geophys. Res.*, B109, B04310, doi:10.1029/2003JB002437, 2004.
- Hargreaves, J. C., and J. D. Annan, Assimilation of paleo-data in a simple Earth system model, *Clim. Dynam.*, 19, 371-381, 2002.
- Johnson, K. M., and P. Segall, Viscoelastic earthquake cycle models of deep stress-driven creep along the San Andreas Fault system, *J. Geophys. Res.*, B, in press, 2004.

Kidd, W. S. F. and P. Molnar, Quaternary and active faulting observed on the 1985 Academia Sinica-Royal Society Geotraverse of Tibet, *Phil. Trans. R. Soc. Lond.*, *327*, 337-363, 1988.

Metropolis, N., A. W. Rosenbluth, M. N. Rosenbluth, A. H. Teller, and E. Teller, Equations of state calculations by fast computing machines, *J. Chem. Phys.*, *21*, 1087-1091, 1953.

Savage, J. C., Viscoelastic-coupling model for the earthquake cycle driven from below, *J. Geophys. Res.*, *B105*, 25,525-25,532, 2000.

Savage, J. C. and W. H. Prescott, Asthenosphere readjustment and the earthquake cycle, *J. Geophys. Res.*, *83*, 3369-3376, 1978.

Scholz, C.H., *The mechanics of earthquakes and faulting*, Cambridge University Press, Cambridge, 439 pp, 1988.

Segall, P., Integrating geologic and geodetic estimates of slip rate on the San Andreas fault system, *Int. Geol. Rev.*, *44*, 62-82, 2002.

Shen, F., L. H. Royden, and B. C. Burchfiel, Large-scale crustal deformation of the Tibetan Plateau, *J. Geophys. Res.*, *B106*, 6793-6816, 2001.

van der Woerd, J., P. Tapponnier, F. J. Ryerson, A.-S. Meriaux, B. Meyer, Y. Gaudemer, R. C. Finkel, M. W. Caffee, G.h. Zhao, and Z.q. Xu, Uniform postglacial slip-rate along the central 600 km of the Kunlun Fault (Tibet), from ²⁶Al, ¹⁰Be, and ¹⁴C dating of riser offsets, and climatic origin of the regional morphology, *Geophys. J. Int.*, *148*, 356-388, 2001.

Wallace, K., G.h. Yin, and R. Bilham, Inescapable slow slip on the Altyn Tagh fault, *Geophys. Res. Lett.*, *31*, L09613, doi:10.1029/2004GH019724, 2004.

Zhang, P.-Z., Z. Shen, M. Wang, W. Gan, R. Brgmann, P. Molnar, Z. Niu, J. Sun, Q. Wang, J. Wu, H. Sun, and X. You, Continuous deformation of the Tibetan Plateau from GPS, *Geology*, in press, 2004.

14. Observations and Modeling of Microseisms in the Santa Clara Valley, California

David Dolenc, Doug Dreger, and Shawn Larsen (LLNL)

14.1 Introduction

Previous studies of the 3D velocity structure in the Santa Clara Valley (SCV) showed that teleseismic, local, and microseism data recorded by the 41-station Santa Clara Valley Seismic Experiment (SCVSE) are all sensitive to basin structure and that they may be used to refine the velocity model of the basins (Dolenc *et al.*, 2004; Dolenc and Dreger, 2004). In our recent work we focused on constraining the source of the microseisms and used this for modeling the microseism observations in the SCV.

14.2 Results

A recent study by Schulte-Pelkum *et al.* (2004) showed that seismic noise in Southern California is highly monodirectional and that the microseisms source can be localized. We have performed a similar analysis by using f-k array method for the data recorded during the SCVSE. Our results show that at low frequencies (0.1 to 0.3 Hz), wavefield observations in the SCV also display directionality (Figure 12.26). At higher frequencies (0.3 to 0.5 Hz), wavefield directionality is lost, which may be due to scattering of the waves by the 3D structure in the SCV basins. The important result of these observations is that the source can be localized and can therefore be used in numerical simulations. We used the 3D finite-difference code E3D (Larsen and Schultz, 1995) and the UCB velocity model (Stidham, 1999; Stidham *et al.*, 1999) to simulate the microseism wavefield. A vertically oriented CLVD source located about 27 km offshore was used to generate isotropic Rayleigh waves. We used the source time function that was a superposition of sine waves at discrete periods over the observed microseismic band. Results for the observed and simulated microseisms are presented in Figure 12.27; both display directionality and source localization for low frequencies.

14.3 Conclusions

The analysis of the observed microseisms in the SCV shows directionality and source localization for low frequencies which enables us to simulate the microseism wavefield. Analysis of simulated waveforms shows agreement with observations in terms of directionality at low frequencies. We plan to refine the method to simulate microseism wavefield by including the source spectrum derived from the ocean wave data recorded at the Santa Cruz buoy. Obtained results will further be used to de-

velop a simultaneous inversion of the teleseismic, local, and microseism observations to constrain the velocity structure of the SCV basins.

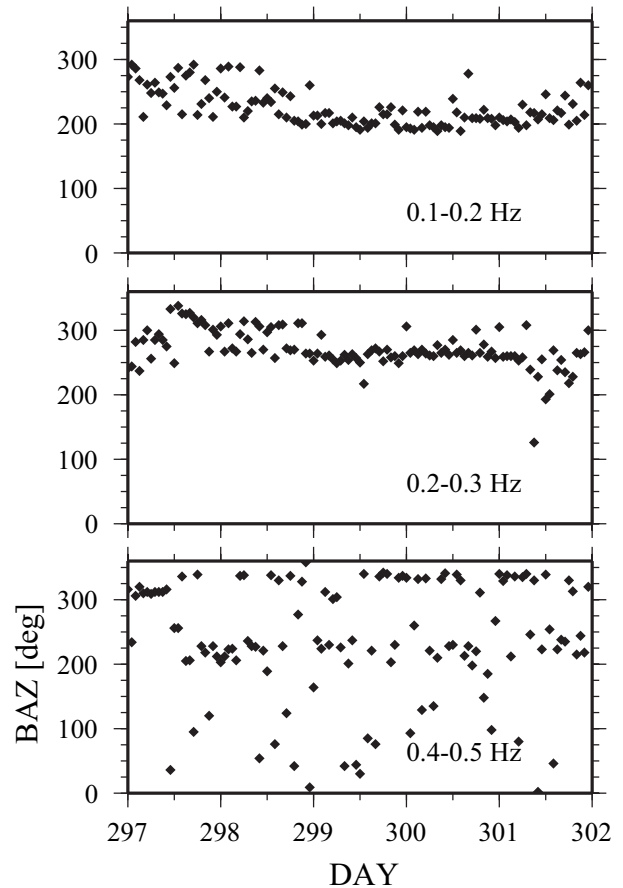


Figure 12.26: Backazimuth of the microseism wavefield over the 5-day period in 1998 determined with the f-k analysis. Results for the three frequency bands are presented.

14.4 Acknowledgements

This research was supported by the USGS grants 03HQGR0003 and 04HQGR0062.

14.5 References

Dolenc, D., D. Dreger, and S. Larsen (2004). Basin structure influences on the propagation of teleseismic

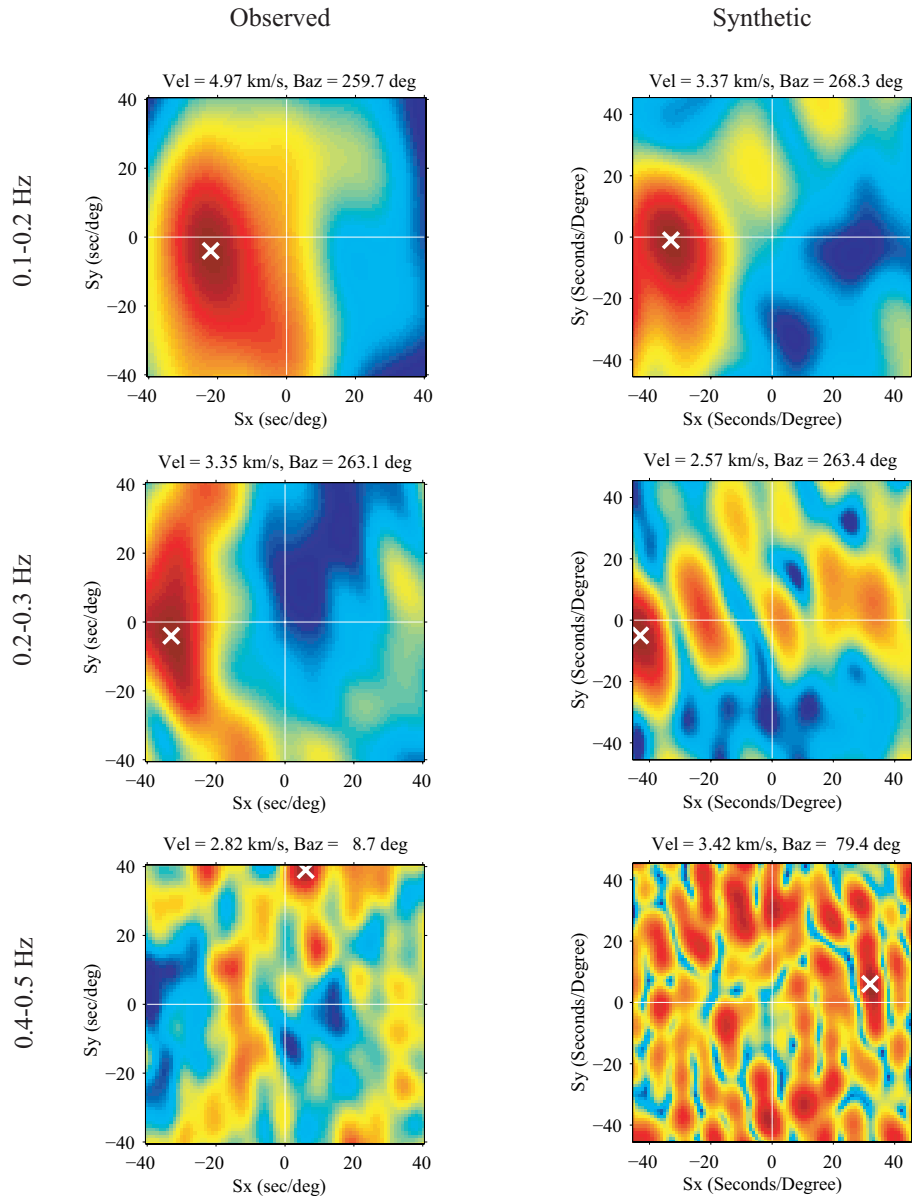


Figure 12.27: Observed (298.1998, 23 UTC) and simulated microseisms in the f - k slowness domain. Crosses indicate maximum power. In both cases, directionality and source localization is observed for low frequencies (0.1 to 0.3 Hz). A color version of this figure may be found on page 154.

waves in the Santa Clara Valley, California, *Bull. Seism. Soc. Am.*, in revision.

Dolenc, D. and D. Dreger (2004). Microseisms observations in the Santa Clara Valley, California, *Bull. Seism. Soc. Am.*, in revision.

Larsen, S. and C.A. Schultz (1995). ELAS3D: 2D/3D elastic finite-difference wave propagation code, Technical Report No. UCRL-MA-121792, 19 pp.

Schulte-Pelkum, V., P.S. Earle, and F.L. Vernon (2004). Strong directivity of ocean-generated seismic noise, *Geochem. Geophys. Geosys.*, 5, Q03004,

doi:10.1029/2003GC000520, 13pp.

Stidham, C., M. Antolik, D. Dreger, S. Larsen, and B. Romanowicz (1999). Three-dimensional structure influences on the strong-motion wavefield of the 1989 Loma Prieta earthquake, *Bull. Seism. Soc. Am.*, 89, 1184-1202.

Stidham, C. (1999). Three-dimensional crustal structure influences on wave propagation and generation of strong ground motion in the greater San Francisco Bay region, *Ph.D. Thesis*, University of California, Berkeley.

15. Excitation of Earth's Incessant Free Oscillations by Atmosphere-Ocean-Seafloor Coupling

Junkee Rhie and Barbara Romanowicz

15.1 Introduction

The "hum" of the earth is well observed on broadband vertical seismic records on days without large earthquakes (Suda *et al.*, 1998). In other words, fundamental mode Rayleigh waves continuously propagate over the whole globe even if there are no significant earthquakes or volcanic eruptions. Its excitation level is similar to the level due to continuous occurrence of events with M_w 5.75 to 6.00. (Ekström, 2001). Since first observation, two competing models for sources of the hum have been proposed; atmospheric random perturbations (Kobayashi and Nishida, 1998) and processes in ocean (Tanimoto, 2003; Rhie and Romanowicz, 2004).

We are here concerned with developing an array-based method to detect and locate the sources of the hum. The array-based method is designed to measure the propagating direction of Rayleigh waves. By using two different arrays in the globe, we can get locations of the energy sources which generate continuous Rayleigh waves propagating through the solid earth. Our results show that Rayleigh wave originates primarily in the northern Pacific Ocean, during northern hemispheric winter, and in the southern oceans during the summer. The location of the sources shift seasonally and have a correlation with the maxima in significant wave height associated with winter storms. Considering our observation, we infer that atmosphere-ocean-seafloor coupling plays a crucial role in generating the "hum" of the Earth. The energy is transferring from storm to solid earth through infragravity waves.

15.2 Method and Observation

As the amplitude of waveform due to the hum is too weak to be detected at any individual recording, amplitude stacking in frequency domain or full great circle anti-dispersion filtering (Ekström, 2001) are used to enhance the signal. Both methods are good to detect the hum but inherently impossible to locate the sources because they are not sensitive to propagating direction of Rayleigh waves at all. To resolve the ambiguity in two competing models, we need to develop the method which is able to locate the sources by taking advantage of propagating properties of Rayleigh waves. An array-based method is a combined method of a traditional beam forming and an anti-dispersion filtering technique. By combining two methods, we can develop an optimal method to detect and measure the propagating direction of the long period (around 240s) surface wave. We used two regional

arrays in Northern California (BDSN) and Japan (F-net). More than 10 quiet stations in each array are selected and then an array-based method is applied on vertical velocity seismograms recorded at those stations. Before applying an array-based method, we need to remove waveforms affected by significant earthquakes because we are only interested in non-earthquake sources. We removed all time windows, which can be affected by events of $M_w > 5.5$. As small events cannot significantly contribute to Rayleigh wave energy above 150s, events with $M_w < 5.5$ are ignored. An array-based method allows us to estimate the distribution of background energy levels of long period Rayleigh waves as a function of time and back azimuth. As we are interested in the long-term average of energy levels, non-symmetric shape of the array can distort the average levels with respect to back azimuth. To overcome this unwanted effect, we just look at the Fourier spectrum of the stack amplitudes as a function of azimuth. If we compare this spectrum to one from synthetic experiment by assuming uniform distribution of sources, we can find that a synthetic spectrum has a negligible "degree one" component, but our observation has a strong degree one component. It indicates that the sources are not uniformly distributed. Here "degree one" means the Fourier component with period of 360 deg.

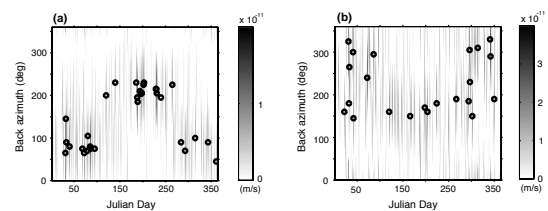


Figure 12.28: Amplitude of degree one as a function of time and back-azimuth for quiet days between 2000 and 2002. A "quiet day" contains at least 12 hours uncontaminated by earthquakes. The quiet day with larger amplitude was selected when we have more than 2 quiet days at same Julian day. (a) Back-azimuth corresponding to the maximum in the degree 1 component of stack amplitude for F-net as a function of time. Black circles indicate maxima with amplitude larger than 1.0×10^{-11} (m/s). (b) same as (a) for BDSN. Amplitude criteria for black circles is 3.0×10^{-11} (m/s)

We considered 3 years of data starting from 2000. One of our final observations is a variation of degree one com-

ponents of average stacks over one day for different Julian days and arrays. Time variation of maximum amplitudes and maximum directions of degree one components of averaged stacks show significant seasonal variation for each season and two arrays point to different regions for summer and winter (Fig. 12.28a,b). Here summer and winter are defined by 6 months from March through September and other 6 months, respectively. By using two maxima directions of degree one components averaged over each season, we can determine the probable regions where the hum originated during each season in 2000 (see Fig. 12.29a,b). We can get similar results for other years.

Two given regions show strong correlation with maxima of significant wave height for summer and winter (Fig. 12.29c,d) and it infers that energy transfer from ocean to solid earth is happening in these regions. However, there is still a possibility that we failed to locate other source regions because the distribution of arrays are too sparse and we are utilizing only first order information of direction to the sources.

15.3 Discussion

Our result implies that the ocean takes an important part in the excitation of the hum. A highly probable scenario of energy transfer from atmosphere to solid earth through oceans is as follows: 1) a significant winter storm generates ocean waves over the mid-latitude oceans; 2) some of the energy leaks out and propagate as free waves into the ocean basins; 3) They interact with the topography of the ocean basin and transfer energy to the solid earth. But the efficiency of generating elastic waves seems to depend on various factors, such as the depth of sea floor, the shape of the continental shelves bounding the ocean basin, and the strength and persistence of storms. For example, the strengths of storms in northern Pacific and northern Atlantic are comparable during northern hemispheric winter, but only northern Pacific seems to generate significant elastic waves, which is in agreement with differences of 20-30dB in pressure noise on the ocean basin between these oceans in the infragravity wave bands (*Webb et al.*, 1999).

15.4 References

Ekström, G., Time domain analysis of Earth's long-period background seismic radiation, *J. Geophys. Res.*, *106*, 26,483-26,493, 2001.

Kobayashi, N., and N. Nishida, Continuous excitation of planetary free oscillations by atmospheric disturbances, *Nature*, *395*, 357-360, 1998.

Rhie, J., and B. Romanowicz, Excitation of earth's incessant free oscillations by atmosphere-ocean-seafloor coupling, *Nature*, **431**, 552-556. 2004.

Suda, N., K. Nawa, and Y. Fukao, Earth's background free oscillations, *Science*, *279*, 2089-2091, 1998.

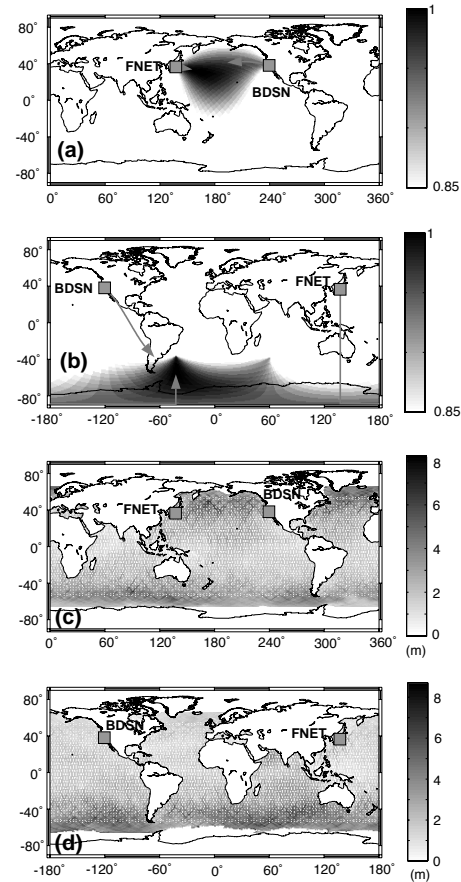


Figure 12.29: Comparison of seasonal variations in the distribution of hum-related noise (degree 1 only) and significant wave height in the year 2000. The directions corresponding to mean amplitudes that are larger than 85 percent of the maximum are combined for the two arrays in winter (a) and in summer (b) to obtain the region of predominant sources in each season. Arrows indicate the direction of maxima. Both arrays are pointing to the Northern Pacific Ocean in the winter and to the southern ocean in the summer. Global distribution of significant wave height, in the winter (c) and in the summer (d), averaged from TOPEX/Poseidon images for the months of January and July, 2000, respectively

Tanimoto, J., Jet stream, roaming ocean waves, and ringing earth, *EOS Trans. AGU* *84*(46), Fall Meet. Suppl., Abstract S12F-04, 2003.

Webb, S., X. Zhang, and W. Crawford, Infragravity waves in the deep ocean, *J. Geophys. Res.*, *96*, 2723-2736, 1991.

16. Episodic Tremor and Slip in the Southern Cascadia Subduction Zone

Mark H. Murray and Bob Uhrhammer

16.1 Introduction

Continuous GPS stations operating over the last decade have begun to detect transient deformation signals from aseismic processes that can occur over hours to days. Deviations from uniform motion of GPS stations in Washington and British Columbia led to the detection of an aseismic 1–2 week slip event on the deeper (25- to 45-km) northern Cascadia subduction zone interface (Dragert *et al.*, 2001). Similar events repeat at 13- to 16-month intervals (Miller *et al.*, 2002), and are also spatially and temporally correlated with pulsating, tremorlike seismic signals with 1–5 Hz frequency content that do not have impulsive onsets (Rogers and Dragert, 2003). One possible explanation for these episodic tremor and slip (ETS) events is that fluids generated by dehydration processes from the slab are playing an important role in regulating the deep slip on the interface (Obara, 2002).

Recent evidence suggest that ETS activity may be occurring along the entire Cascadia subduction zone (Szeliga *et al.*, 2004). We are assessing our GPS and seismic observations to provide better constraints on this behavior in northern California.

16.2 Results

The daily position time series at Yreka (YBHB) (Figure 12.30) shows evidence for cm-level transient deformation lasting 1–2 weeks that is similar to the behavior detected in northern Cascadia. We have developed a detection algorithm, based on a smoothed, 10-day running median of hourly power spectral density estimates in the 1–5 Hz range, and have applied this algorithm to Yreka (YBH) seismic data from 2000–2004. The high peaks (Figure 12.30) correspond to periods when the tremor noise dominates the signals, and these peaks are highly correlated with the episodic westward GPS displacements. The peaks have a 10.9 ± 2.0 month period (shorter than the 14 month period found near Puget Sound). The correlations are less clear on the north GPS component. Episodic displacements at these frequencies have not been observed on the coastal continuous GPS stations, so currently the YBHB GPS observations and the corresponding tremors observed at YBH and other northern California stations provide the only evidence for episodic slow earthquakes in the southern Cascadia subduction zone. We are currently studying tremors detected on other seismic instruments and improving our GPS regional filtering techniques to better characterize the possible deformation signals.

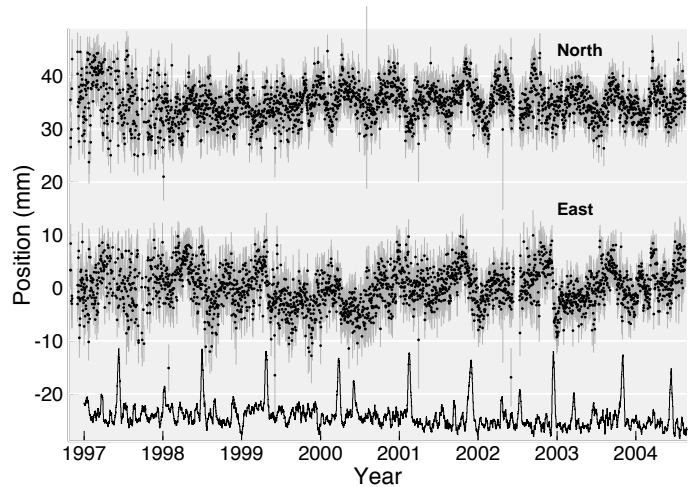


Figure 12.30: Timeseries of YBHB daily north and east positions, with standard errors, estimated using GAMIT. Long-term average motion and annual sinusoidal signals have been removed. Black lines are the smoothed hourly median power spectral density estimates in the 1–5 Hz pass band at the YBH BDSN station, with higher values during periods of strong seismic tremor. The episodic GPS deformation, particularly on the east component, is strongly correlated with tremor periods, suggesting that episodic slow earthquakes may be occurring along the southern Cascadia subduction zone.

16.3 References

- Dragert, H., K. Wang, and T. S. James, A silent slip event on the deeper Cascadia subduction interface, *Science*, 292, 1525–1528, 2001.
- Miller, M. M., T. Melbourne, D. J. Johnson, W. Q. Sumner, Periodic slow earthquakes from the Cascadia subduction zone, *Science*, 295, 2423, 2002.
- Obara, K., Nonvolcanic deep tremor associated with subduction in southwest Japan, *Science*, 296, 1679–1681, 2002.
- Rogers, G., and H. Dragert, Episodic tremor and slip: The chatter of slow earthquakes, *Science*, 300, 1942–1944, 2003.
- Szeliga, W., T. I. Melbourne, M. M. Miller, and V. M. Santillan, Southern Cascadia episodic slow earthquakes, *Geophys. Res. Lett.*, 31, L16602, doi:10.1029/2004GL020824, 2004.

17. A Three Dimensional Radially Anisotropic Model of Shear Velocity in the Whole Mantle

Mark Panning and Barbara Romanowicz

17.1 Introduction

The 3D seismic velocity structure of the Earth’s mantle represents a snapshot of its current thermal and chemical state. As tomographic models of the isotropic seismic velocity converge in their main features (*Masters et al., 2000; Mégnin and Romanowicz, 2000; Ritsema and van Heijst, 2000; Gu et al., 2001*), geodynamicists use them to infer the density structure, and thus the buoyancy contrasts which drive mantle convection (*Hager, 1984; Ricard and Vigny, 1993; Daradich et al., 2003*). This process, however, is complicated by the difficulty of separating thermal and chemical contrasts, and the lack of direct sensitivity of seismic velocities to the density contrasts which drive the convection.

In many regions of the mantle, analyzing the anisotropy of seismic velocities can give us another type of constraint on mantle dynamics. Nearly all the constituent minerals of the mantle have strongly anisotropic elastic properties on the microscopic scale. Random orientations of these crystals, though, tend to cancel out this anisotropy on the macroscopic scale observable by seismic waves, unless crystals or materials with strongly contrasting elastic properties are aligned through deformation processes. While in the relatively cold regions of the lithosphere these anisotropic signatures can remain frozen in over geologic time-scales (*Silver, 1996*), observed anisotropy at greater depths likely requires dynamic support (*Vinnik et al., 1992*). Thus, the anisotropy observed at sub-lithospheric depths is most likely a function of the current mantle strain field, and these observations can help us map out mantle flow.

17.2 Model Results

We have developed a degree 16 3D radially anisotropic shear velocity model of the whole mantle using a large three component surface and body waveform dataset and an iterative inversion for structure and source parameters based on Nonlinear Asymptotic Coupling Theory (NACT) (*Li and Romanowicz, 1995*). The model is parameterized in terms of isotropic V_S and an anisotropic parameter, ξ , which is defined by $\xi = V_{SH}^2/V_{SV}^2$. The model shows a link between mantle flow and anisotropy in a variety of depth ranges.

The common features of S tomographic models are present in the isotropic V_S model. The uppermost 200 km is dominated by tectonic features, with fast continents and slower oceans that show an age-dependent increase in velocity away from the slow velocities near ridges. Re-

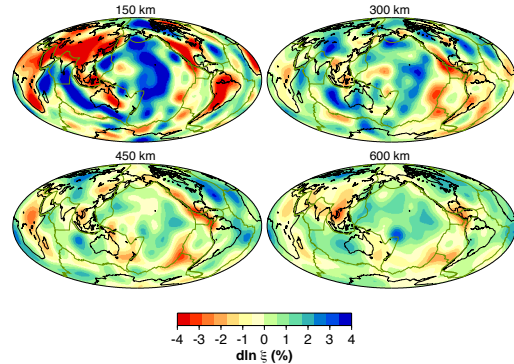


Figure 12.31: ξ structure at four depths in the upper mantle and transition zone.

gions of active tectonic processes are, in general, slower, such as western North America, the major circum-Pacific subduction zones, and the East African rifting. In the transition zone depth range, the most prominent features are the fast velocities of subducted slabs, while the slow ridges are no longer present. Mid-mantle velocity anomalies are low in amplitude, and more white in spectrum. Finally, in the lowermost 500 km, the amplitudes of heterogeneity increase again, and become dominated by a degree 2 pattern with rings of higher velocities surrounding two lower velocity regions under the central Pacific and Africa, commonly referred to as superplumes.

In the ξ model of the upper mantle (Figure 12.31), we confirm observations of regions with positive ξ anomalies ($V_{SH} > V_{SV}$) starting at ~ 80 km under oceanic regions and ~ 250 km under old continental lithosphere, suggesting horizontal flow beneath the lithosphere (*Gung et al., 2003*). We also observe a $V_{SV} > V_{SH}$ signature at ~ 200 -300 km depth beneath major ridge systems with amplitude correlated with spreading rate. In the transition zone (400-700 km depth), regions of subducted slab material are associated with negative ξ anomalies ($V_{SV} > V_{SH}$) (Figure 12.31), while the ridge signal decreases except under the East Pacific Rise.

We also confirm the observation of strong radially symmetric $V_{SH} > V_{SV}$ in the lowermost 300 km (Figure 12.32) (*Panning and Romanowicz, 2004*). The 3D deviations from this degree 0 signature are associated with

the transition to the large-scale superplumes under the central Pacific and Africa, suggesting that $V_{SH} > V_{SV}$ is generated in the predominant horizontal flow of a mechanical boundary layer, with a change in signature related to transition to upwelling at the superplumes.

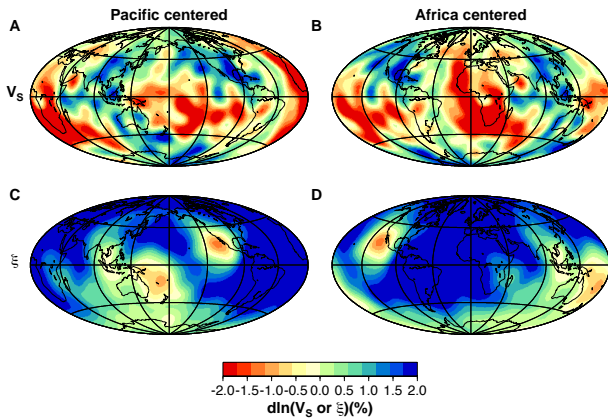


Figure 12.32: Isotropic V_S (top) and ξ (bottom) structure at 2800 km depth, centered under the Pacific (left) and Africa (right).

17.3 Source Inversions

In the process of developing the anisotropic model, we also invert for source parameters for the events in our dataset, starting from published Harvard CMT solutions, which are developed in a simpler mantle velocity model. We performed an iterative inversion, with scalar seismic moment fixed. 964 of the 1191 events in our dataset had sufficient data coverage for a stable inversion which showed an improvement in fit. While changes in mechanism and location were quite small (horizontal location shifts averaged 0.015°), there was evidence for systematic relocation due to the improved structural model, particularly in the circum-Pacific subduction zones (Figure 12.33).

17.4 References

Daradich, A., J.X. Mitrovica, R.N. Pysklywec, S.D. Willett and A.M. Forte, Mantle flow, dynamic topography, and rift-flank uplift of Arabia, *Geology*, **30**, 901-904, 2003.

Gu, Y.J., A.M. Dziewonski, W. Su, and G Ekström, Models of the mantle shear velocity and discontinuities in the pattern of lateral heterogeneities, *J. Geophys. Res.*, **106**, 11,169-11,199, 2001.

Gung, Y., M. Panning and B. Romanowicz, Global anisotropy and the thickness of continents, *Nature*, **422**, 707-711, 2003.

Hager, B.H., Subducted slabs and the geoid - constraints on mantle rheology and flow, *J. Geophys. Res.*,

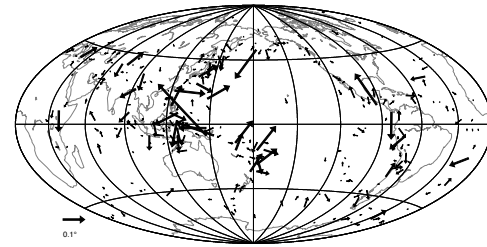


Figure 12.33: Vector-summed event relocations in $5^\circ \times 5^\circ$ cells.

89, 6003-6015, 1984.

Li, X.D. and B. Romanowicz, Comparison of global waveform inversions with and without considering cross-branch modal coupling, *Geophys. J. Int.*, **121**, 695-709, 1995.

Masters, G., G. Laske, H. Bolton and A. Dziewonski, The relative behavior of shear velocity, bulk sound speed, and compressional velocity in the mantle: implications for chemical and thermal structure, in *Earth's Deep Interior*, AGU Monograph 117, pp. 63-86, eds. Karato, S., A.M. Forte, R.C. Liebermann, G. Masters and L. Stixrude, Amer. Geophys. Union, Washington, D.C., 2000.

Mégnin, C., and B. Romanowicz, The 3D shear velocity of the mantle from the inversion of body, surface, and higher mode waveforms, *Geophys. J. Int.*, **143**, 709-728, 2000.

Panning, M.P. and B. Romanowicz, Inferences on flow at the base of Earth's mantle based on seismic anisotropy, *Science*, **303**, 351-353, 2004a.

Ricard, Y. and C. Vigny, Mantle dynamics with induced plate tectonics, *J. Geophys. Res.*, **94**, 17,543-17,560, 1989.

Ritsema, J. and H.-J. van Heijst, Seismic imaging of structural heterogeneity in Earth's mantle: evidence for large-scale mantle flow, *Science Progress*, **83**, 243-259, 2000.

Silver, P.G., Seismic anisotropy beneath the continents: probing the depths of geology, *Annu. Rev. Earth Planet. Sci.*, **24**, 385-432, 1996.

Vinnik, L.P., L.I. Makeyeva, A. Milev and Y. Usenko, Global patterns of azimuthal anisotropy and deformations in the continental mantle, *Geophys. J. Int.*, **111**, 433-447, 1992.

18. High Resolution Anisotropic Structure of the North American Upper Mantle from Inversion of Body and Surface Waveform Data

Federica Marone, Yuancheng Gung and Barbara Romanowicz

18.1 Introduction

Seismic anisotropy is required for a correct interpretation of the retrieved S -velocity structure in tomographic studies at least in the first 400 km of the upper mantle (Gung *et al.*, 2003). A detailed knowledge of the seismic anisotropic structure of the earth's mantle also provides insight into debated geophysical issues, such as the nature and strength of lithosphere/asthenosphere coupling, the depth extent of continental sub-regions and the relation of imaged seismic anisotropy to present-day asthenospheric flow and/or past tectonic events recorded in the lithosphere.

To date, our knowledge of the North American anisotropic structure arises mainly from global tomographic models (e.g. Ritsema *et al.*, 1999; Gung *et al.*, 2003) or SKS splitting studies (e.g. Fouch *et al.*, 2000; Savage and Sheehan, 2000), which lack horizontal and vertical resolution respectively, and are limited to either radial or azimuthal anisotropy.

Our goal is a new high resolution model for the North American upper mantle incorporating both radial and azimuthal anisotropy. We aim at unprecedented lateral and depth resolution by improving both data coverage and methodology.

18.2 Dataset

We have collected and processed 3 component body, fundamental and higher mode surface waveforms to complement the BSL database and improve the data coverage for North America. In particular, we focused our attention to broad band seismograms recorded at the numerous permanent seismic stations deployed throughout North America (Figure 12.34), from events at teleseismic and far regional distances. From each deconvolved and filtered seismogram, individual body and surface wave energy packets have been extracted using an automated selection algorithm and subsequently checked by hand, to ensure a high quality dataset. The compiled data collection consists of more than 100,000 3 component body, fundamental and higher mode surface waveforms and provides a fairly homogeneous path (Figure 12.34) and azimuthal coverage.

We plan to use independent information from SKS splitting measurements as additional constraints on the anisotropic model.



Figure 12.34: Data coverage - Paths of teleseismic events with $M_w \geq 6$ recorded at North American stations (indicated by white triangles), for which high quality fundamental mode Rayleigh wavepackets have been selected.

18.3 Methodology Improvements

We invert seismic long period waveform data in the framework of normal mode asymptotic theory (NACT - Li and Romanowicz, 1996). The resulting broad band sensitivity kernels allow us to exploit the information contained in long period seismograms for body, fundamental and higher mode surface waves simultaneously.

Until now, this approach has only been applied at the global scale with lateral parametrization in terms of spherical harmonics (Li and Romanowicz, 1996; Mégnin and Romanowicz, 2000). We have adapted the procedure to the regional case by implementing a lateral parametrization in terms of spherical splines on an inhomogeneous triangular grid of knots (e.g. Wang and Dahlen, 1995), with the finest mesh for the region of interest, where the data coverage is densest, and a coarser grid outside the studied region (Figure 12.35).

Body and surface wave datasets used in mantle seismic tomography are sensitive to crustal structure, but cannot resolve details within the crust. Accurate crustal corrections are therefore essential for the quality of high resolution regional tomographic studies. The effect of shallow-layer features is often removed from the data by assuming an a priori crustal model (e.g. CRUST2.0) and applying

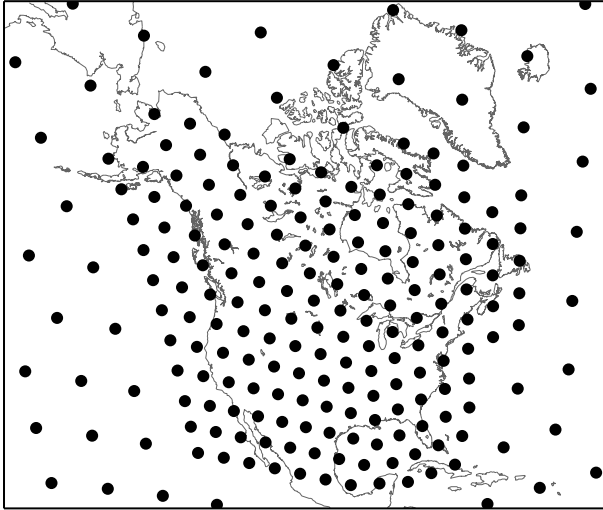


Figure 12.35: Example of irregular grid with a finer mesh for North America

linear perturbation corrections. However, lateral variations in Moho depth can be fairly large even over short distances, as for instance at ocean/continent transitions and the adequacy of linear corrections is questionable. In fact, *Montagner and Jobert (1988)* showed that the non-linearity of shallow-layer corrections is often non negligible even at long periods. In high resolution upper mantle regional tomographic studies, it is therefore important to take the crustal structure into account in a more accurate way. Going beyond the linear perturbation approximation, we follow the approach proposed by *Montagner and Jobert (1988)* and split the correction into a linear and non-linear part. At each point along a path, we assign a 1D reference model according to the local crustal structure (e.g. extended crust, orogen, ocean, ...). We then correct for the difference between the discontinuities in the chosen a priori crustal model (e.g. CRUST2.0) and the selected 1D local reference model assuming a linear perturbation, and exactly for the difference, if any, between the local reference model and PREM (our global reference model).

18.4 Future of the Project

Preliminary inversions of the compiled dataset using the improved NACT algorithm resulted in a radial anisotropic upper mantle structure reproducing the major features shared by all recent models (e.g. *Ritsema et al., 1999*; *Gung et al., 2003*), such as high velocities beneath cratons between 100 and 250 km depth and negative velocity anomalies in back arc regions. While refining this preliminary model, we will work on the next step and implement a more complete anisotropic parametrization. Our final goal is a model incorporating both radial and

azimuthal anisotropy. Such a model can be parametrized in terms of radial anisotropy with a symmetry axis of arbitrary orientation, corresponding to the 5 Love parameters plus two angles defining the axis orientation. The backbone permanent network component of USArray, complemented by temporary Big Foot deployments, will provide an unprecedented density of recordings. This unique dataset will guarantee the resolution of this increased number of parameters.

18.5 Acknowledgements

This work has been financially supported by the Swiss foundation “Stefano Franscini”.

We are grateful to the IRIS Data Management Center (DMC) as well as to the Geological Survey of Canada for providing waveform data used in this study.

18.6 References

- Fouch, M.J., K.M. Fischer, E.M. Parmentier, M.E. Wysession and T.J. Clarke, Shear-wave splitting, continental keels, and patterns of mantle flow, *J. Geophys. Res.*, *105*, 6255-6275, 2000.
- Gung, Y., M. Panning and B. Romanowicz, Global anisotropy and the thickness of continents, *Nature*, *422*, 707-711, 2003.
- Li, X.D. and B. Romanowicz, Global mantle shear-velocity model developed using nonlinear asymptotic coupling theory, *Geophys. J. R. Astr. Soc.*, *101*, 22,245-22,272, 1996.
- Mégnin, C. and B. Romanowicz, The 3D shear velocity structure of the mantle from the inversion of body, surface and higher mode waveforms, *Geophys. J. Int.*, *143*, 709-728, 2000.
- Montagner, J.-P. and N. Jobert, Vectorial tomography; II. Application to the Indian Ocean, *Geophys. J.*, *94*, 309-344, 1988.
- Ritsema, J., H. van Heijst and J. Woodhouse, Complex shear wave velocity structure imaged beneath Africa and Iceland, *Science*, *286*, 1925-1928, 1999.
- Savage, M.K. and A.F. Sheehan, Seismic anisotropy and mantle flow from the Great Basin to the Great Plains, western United States, *J. Geophys. Res.*, *105*, 13,715-13,734, 2000.
- Wang, Z. and F. Dahlen, Spherical-spline parametrization of three-dimensional Earth models, *Geophys. Res. Lett.*, *22*, 3099-3102, 1995.

19. Tests of Normal Mode Asymptotic Approximations against Computation Using the Spectral Element Method

Yuancheng Gung, Barbara Romanowicz and Yann Capdeville

19.1 Introduction

We evaluate normal mode asymptotic methods by comparing the corresponding 3D synthetics with those computed using the coupled spectral element/normal mode method (CSEM) (Capdeville *et al.*, 2003). Three normal mode based asymptotic approaches are compared: (1) path average approximation (PAVA) (Woodhouse and Dziewonski, 1984), in which only along-branch mode coupling effects are considered; (2) Non-linear asymptotic coupling theory (NACT) (Li and Romanowicz, 1995), which includes the across-branch mode coupling effects; and (3) NACT+F, an extension of NACT with focusing terms computed using higher order asymptotic theory (Romanowicz, 1987; Romanowicz *et al.*, 2004). Systematic waveform comparisons are implemented. We find that NACT and NACT+F provide much better fit, and the off-great-circle effects, which result in focusing/defocusing and not seen by PAVA or NACT, are well explained by NACT+F.

19.2 Experiments and Results

Two 3-D synthetic Earth models are used to test the validity of three normal mode based analytical approaches, PAVA, NACT and NACT+F. The CSEM is used to provide the accurate reference synthetics in the 3-D test models.

The synthetic models are parameterized laterally using spherical harmonics up to degree 16, and radially using cubic splines. To examine more closely the small perturbation of the seismograms caused by the 3-D heterogeneities, the differential waveforms (i.e. $\mathbf{u}_{3D \text{ model}} - \mathbf{u}_{\text{reference model}}$) for CSEM and normal mode techniques are compared. Two representative results are shown here. Figure 12.36 shows the results for an isotropic source in a 3-D model with an ellipsoidal anomaly centered at the 220 km depth, and Figure 12.37 shows the results for a dip-slip source in a 3-D model with two opposite ellipsoidal anomalies centered at 150 km depth.

From the above results, we find that (1) when the path just grazes the anomaly, both PAVA and NACT fail to match CSEM synthetics, since they are insensitive to off-path structure, while NACT+F predicts the expected focusing effects fairly well; and (2) when the path passes through two anomalies with opposite signs, the effects of heterogeneities are cancelled out in the PAVA formalism (there is nearly no perturbation in PAVA differential waveform, as seen in Figure 12.37), and they are well

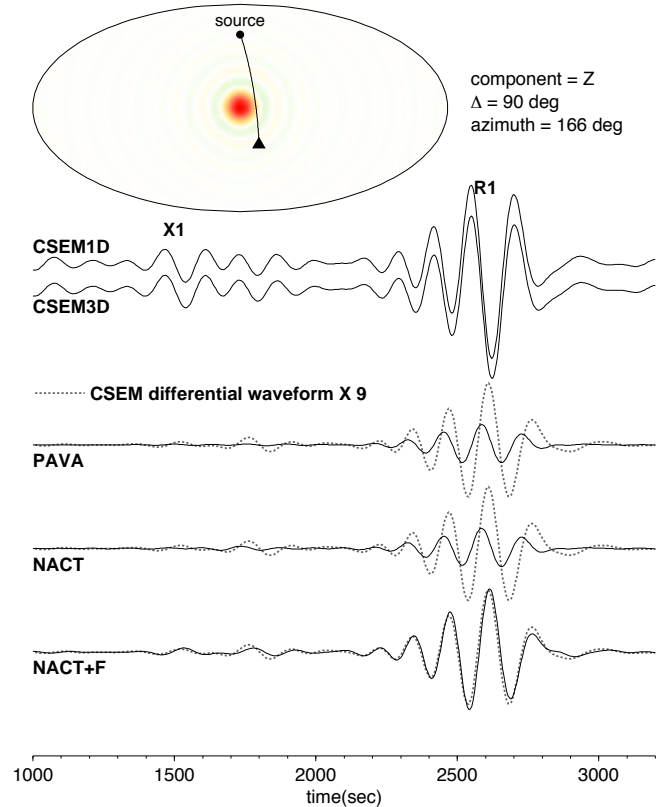


Figure 12.36: Top map: the geometrical relation of the isotropic source (black dark circle), the surface receiver (triangle) and lateral variations of hypothetical 3-D model, a slow velocity anomaly of maximum amplitude -5% at 220 km depth. Top trace: CSEM synthetics for the reference model (CSEM1D) and for the 3-D model (CSEM). In the bottom panels, the differential waveforms of CSEM (dashed line) and three normal mode based asymptotic approaches (solid line) are compared. Note that in this particular case, the great circle path just grazes the anomaly.

20. Finite Boundary Perturbation Theory for the Elastic Equation of Motion

Nozomu Takeuchi

20.1 Introduction

The crust is the most heterogeneous region of the Earth, and accurate crustal correction (i.e., accurate computation of the perturbation of synthetic seismograms caused by the crustal heterogeneities) is critical for obtaining accurate mantle structure models. The heterogeneities are usually represented by the summation of (i) the perturbation of physical properties (such as density and elastic constants) in the internal regions and (ii) the perturbation of the location of the boundaries (such as Moho and the surface), and the principal difficulty is how to compute the effect of the latter perturbation.

The computational method applied to the actual waveform inversion studies for global 3-D Earth structure thus far has been either the modal summation method (e.g., *Li and Tanimoto, 1993*) or the Direct Solution Method (e.g., *Takeuchi et al., 2000*). Both methods solve the weak form equation of motion (or its equivalence) and use vector spherical harmonics as the laterally dependent part of the trial functions. For those global trial functions, severe limitations still exist in computing the perturbation of synthetic seismograms caused by the perturbation in the location of the boundaries, because previous solutions rely on the first order perturbation theory of the free oscillation (hereafter referred as 1DT; *Woodhouse, 1980*). Thus, this method breaks down for strongly heterogeneous medium or for higher frequencies.

In this study, we derive the exact weak form equation of motion for the medium with finite boundary perturbations. This method can be applied to arbitrary trial functions; that is, to both global and local trial functions. We can solve the derived equation of motion by either direct solution or higher order perturbation approximations, which allows highly accurate synthetic seismograms. Hereafter we refer this solution as the finite boundary perturbation theory or FPT.

20.2 Numerical Examples

We show that in the simulations of realistic problems, a breakdown can be observed in 1DT synthetic seismograms. We consider a plane of a great circle including the path shown by the solid line in Figure 12.38a, and simulate SH waves propagating on this plane.

We compute synthetic seismograms for the initial model (isotropic PREM) and the perturbed model (Figure 12.38b), and show the record sections in Figure 12.39. For the perturbed model, we compute by using FPT and 1DT, respectively. We apply a band pass filter with the

corner frequencies of 1/1000 and 1/50 Hz. In the record section for the initial model (Figure 12.39 left), as well as the body waves observed at the first motion part, we observe the Love waves traveling at a speed of about 4.4 km/s (aligning almost straight in the record section). Their waveforms are almost one wave packet and do not clearly show dispersion. On the other hand, in the record section computed for the perturbed model by using FPT (Figure 12.39 middle), we observe Love waves with clear dispersion. This is a well-known feature of Love waves traveling through a continent. However, in the record section computed for the perturbed model by using 1DT (Figure 12.39 right), we cannot clearly see dispersion, an indication that 1DT breaks down for this frequency range.

20.3 Discussion

In the numerical examples we showed that 1DT breaks down for surface waves with a period of 50 seconds in a realistic problem. In recent waveform inversion studies (e.g., *Mégnin and Romanowicz, 2000*; *Takeuchi and Kobayashi, 2004*), the body waves for this frequency range are used as a data set, but the surface waves for this frequency range are excluded. This is mainly due to the insufficient accuracy of 1DT for computing the effect of crustal heterogeneities. Our method can compute accurate synthetic seismograms for arbitrary frequency ranges, and should be better able to retrieve the information in the surface waves of higher frequencies.

20.4 Acknowledgements

This research was partly supported by grants from the Japanese Ministry of Education, Culture, Sports, Science, and Technology (No. 16740249).

20.5 References

- Bassin, C., G. Laske, and G. Masters, The current limits of resolution for surface wave tomography in North America, *EOS Trans. Amer. Geophys. Un.*, *81*, F897, 2000.
- Li, X.D. and T. Tanimoto, Waveforms of long-period body waves in a slightly aspherical Earth model, *Geophys. J. Int.*, *112*, 92-102, 1993.
- Mégnin, C. and B. Romanowicz, The three-dimensional shear velocity structure of the mantle from the inversion of body, surface and higher-mode waveforms, *Geophys. J. Int.*, *143*, 709-728, 2000.

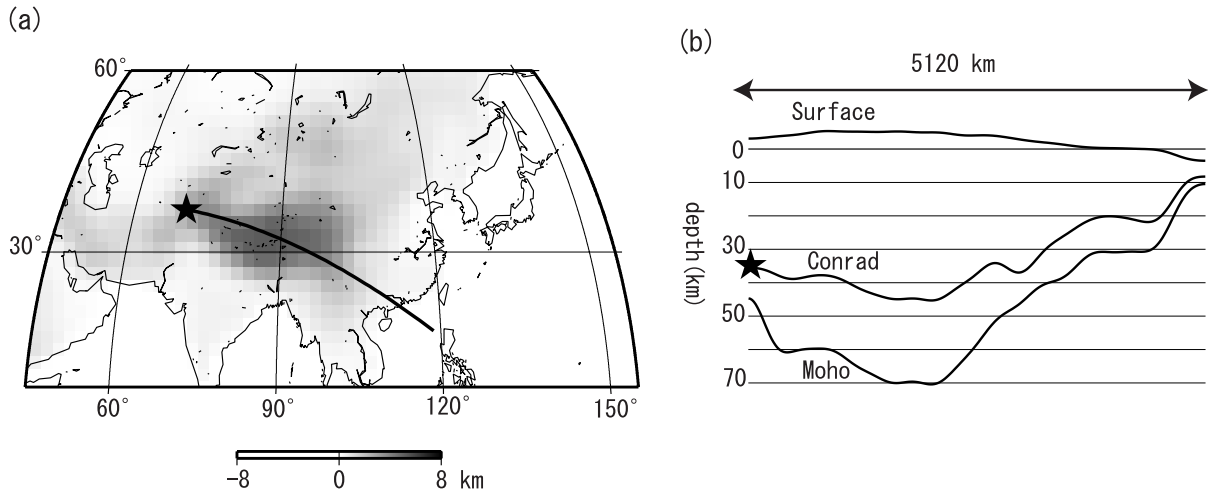


Figure 12.38: (a) The path on which the SH wave propagations are simulated (thick solid line). The star shows the location of the source. Surface (or bathymetry) topography of Crust 2.0 model (Bassin *et al.*, 2000) are overlapped by black-and-white color scale. (b) The crustal topography model used as the perturbed model in this simulation to represent the Crust 2.0 model on the thick solid line in Figure 12.38a. The star shows the location of the source used with this perturbed model.

Takeuchi, N., R.J. Geller and P.R. Cummins, Complete synthetic seismograms for 3-D heterogeneous Earth models computed using modified DSM operators and their applicability to inversion for Earth structure, *Phys. Earth and Plan. Int.*, 119, 25-36, 2000.

Takeuchi, N. and M. Kobayashi, Improvement of Seismological Earth Models by Using Data Weighting in Waveform Inversion, *Geophys. J. Int.*, 158, 681-694, 2004.

Woodhouse, J.H., The coupling and attenuation of nearly resonant multiplets in the Earth's free oscillation spectrum, *Geophys. J. R. Astr. Soc.*, 61, 261-283, 1980.

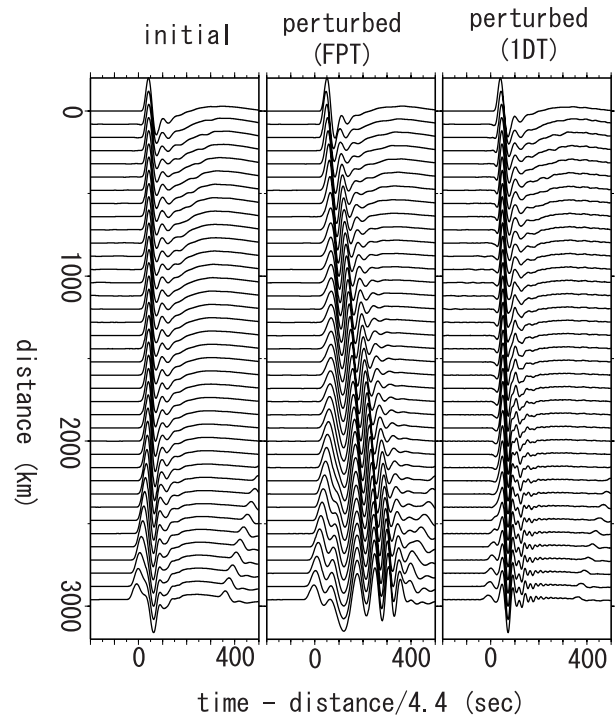


Figure 12.39: The record section computed for the initial model (left), for the perturbed model by using FPT (middle), and for the perturbed model by using 1DT (right). The vertical axis shows the distance from the epicenter, and the horizontal axis shows the reduced time by 4.4^{-1} s/km. The amplitude is normalized by the maximum amplitude of each trace.

21. Sharp lateral Boundaries in the D'' Region

Akiko To and Barbara Romanowicz

21.1 Introduction

Global shear velocity tomographic models show the existence of two superplumes lying in the lower mantle. The large-scale low velocity structures are observed under southern Africa and the mid-Pacific (*Romanowicz*, 2003). Recently, sharp lateral transitions in the velocity structure have been reported at the borders of the African superplume (*Ni et al.*, 2002) and Northeast side of the Pacific superplume (*Bréger and Romanowicz*, 1998). Here we report that a sharp lateral boundary also exists at the southern edge of the Pacific superplume. The set of SHdiff waveforms, which graze the South Pacific, have similar features to those observed at the southeastern edge of the African superplume. The arrival time shifts rapidly, with the emergence of multiple pulses, depending on the azimuth. The coupled mode/spectral element method (CSEM in what follow) (*Capdeville et al.*, 2003) is used to construct synthetic waveforms. We show the first order features of these waveforms from Africa and the South Pacific can be produced by a very simple structure model with strong, sharp lateral heterogeneity lying almost parallel to the ray paths.

21.2 Data and Modeling

Figure 12.40(a) shows the locations of the events and stations. Only deep earthquakes (depth > 450 km) are used. Figure 12.40(b) left panel shows the SHdiff waveforms which graze southeastern edge of African anomaly (hereafter AFA) recorded at the Tanzanian array. They are also shown in other studies (*Wen*, 2001; *Ni and Helmberger*, 2004). Figure 12.40(b) right panel shows the SHdiff records of Fiji-Tonga events recorded at the station BDFB Brazil. They graze the Southern part of Pacific slow velocity anomaly region (hereafter PSA). These two sets of SHdiff waveform, are very similar in the following ways. First of all, the onset times of the first arrivals show large delay as the raypath enter the slow region that lies on the northern part. The first arrivals shift about 20 seconds and 12 seconds in the case of AFA and SPA respectively. Second, the waveforms, which graze the transition show an additional pulse indicated with red lines in Figure 12.40(b). This later phase is the feature we model in the following section. The travel time shift observed in PSA is due to a heterogeneity at the base of the mantle, because the differential travel times measurements of Sdiff-SKKS increase steeply for 8 seconds with respect to the back azimuth.

We used a coupled mode and spectral element method for the waveform modeling. The spectral element method

is most appropriate technique at present, because it can handle 1) the propagation of seismic waves in 3D models with strong lateral variations and in spherical geometry and 2) diffracted waves along the core mantle boundary. The drawback of the method is the large numerical cost. The CSEM is a hybrid method that couples spectral element computations with a normal mode solution, so that the spectral element method is used only in the target strongly heterogeneous regions, which is the bottom 370km of the mantle in this study. We compute the synthetic waveforms down to 12 seconds with a corner frequency at 18 seconds. The model has the 1D structure of PREM (*Dziewonski and Anderson*, 1981) down to a depth of 2591 km, and the 3D model below 2591km, down to the CMB. The model of the 3D part is shown in Figure 12.40(c). The boundaries are displaced 15 degrees from the great circle (shown by a yellow line) that goes through the source.

Figure 12.40(d) shows the synthetic waveforms constructed by CSEM. Each trace is normalized by its maximum amplitude. The source is located on the fast side in Figure 12.40(d) left panel and slow side in the right panel. Multiple pulses are observed in both cases. The possible explanation for each pulse is shown in the caption.

According to the tomographic models, the configurations of the raypaths and the interface of the observed cases are likely to be those of Figure 12.40(d) left panel. The synthetic waveforms capture the following features of the observations: 1) they consist of multiple pulses in the transition region 2) when moving from the fast to the slow region, the arrival of the first and last pulses become closer and finally merge for the stations located in the slow region. This feature is observed more clearly in AFA case, but can only be suggested in PSA case.

The observed and synthetic waveforms are presented in different time scale and frequency ranges, to show the qualitative similarity between the waveforms. The time scale of the synthetics is much larger than that of the observed waveforms. However, this is because of the frequency limitation of the present SEM calculations, which is dictated by the computer power available to us. Calculations of the CSEM synthetics to higher frequencies would allow a better separation of these pulses for paths close to the vertical boundary, as seen in the observations. We also note that only a 3% velocity jump is sufficient to explain the observed time shift of 20 sec in AFA. A large contrast of 6% at the boundary is chosen in the models in order to observe each pulse clearly, since a smaller velocity contrast makes the amplitude of the second pulse

much smaller.

neath the Indian Ocean. *Earth Planet. Sci. Lett.*, **194**, pp.,2002

21.3 Discussion and Conclusion

When the wavepath in the D" is quasi-parallel to a sharp vertical boundary, the Sdiff waveforms are accompanied by secondary phases (red lines in Figure 12.40(b) and Figure 12.40(d)). The synthetic tests from the models of Figure 12.40(c) give only a qualitative constraint on the model, which is the existence of a sharp lateral boundary in the D" region. However, because SEM includes the 3D effects from strong heterogeneous structures, the order of magnitude of the effects to the waveforms is well captured with the simple model.

We show that sharp lateral boundaries, which rise almost like a vertical wall, exist not only in the border of the African plume but also under the south Pacific. This indicates that the low velocity region in the lower mantle under Pacific and Africa, observed as the strong degree-2 pattern in shear velocity tomographic models, have the similar nature also in the finer scales. Unlike the African superplume where the shape and the location of much of the boundaries are revealed, large uncertainty remains in the shape of the Pacific superplume.

21.4 Acknowledgements

We thank the National Science Foundation for support of this research.

21.5 References

Bréger L. and B. Romanowicz, Three-dimensional structure at the base of the mantle beneath the central Pacific. *Science*, **282**, pp. 718-720,1998.

Capdeville, Y., A. To and B. Romanowicz, Coupling spectral elements and modes in a spherical earth: an extension to the "sandwich" case, *Geophys. J. Int.*, **154**, 44-57, 2003

Dziewonski A.M. and D.L. Anderson, Preliminary reference Earth model. *Phys. Earth Planet. Inter.*, **25**, pp. 297-356,1981.

Mégnin C. and B. Romanowicz, The three-dimensional shear velocity structure of the mantle from the inversion of body, surface and higher-mode waveforms. *Geophys. J. Int.*, **143**, pp. 709-728,2000.

Ni S. and D. Helmberger, Seismic Modeling Constraints on the South African Superplume *draft* 2004

Ni S., E. Tan, M. Gurnis and D.V. Helmberger, Sharp sides to the African super plume. *Science* **296**, pp. 1850-1852,2002.

Romanowicz B, Global Mantle Tomography: Progress Status in the Past 10 Years *Annu. Rev. Earth Planet. Sci.*, **31** 303-328, 2003

Wen L., Seismic evidence for a rapidly varying compositional anomaly at the base of the Earth's mantle be-

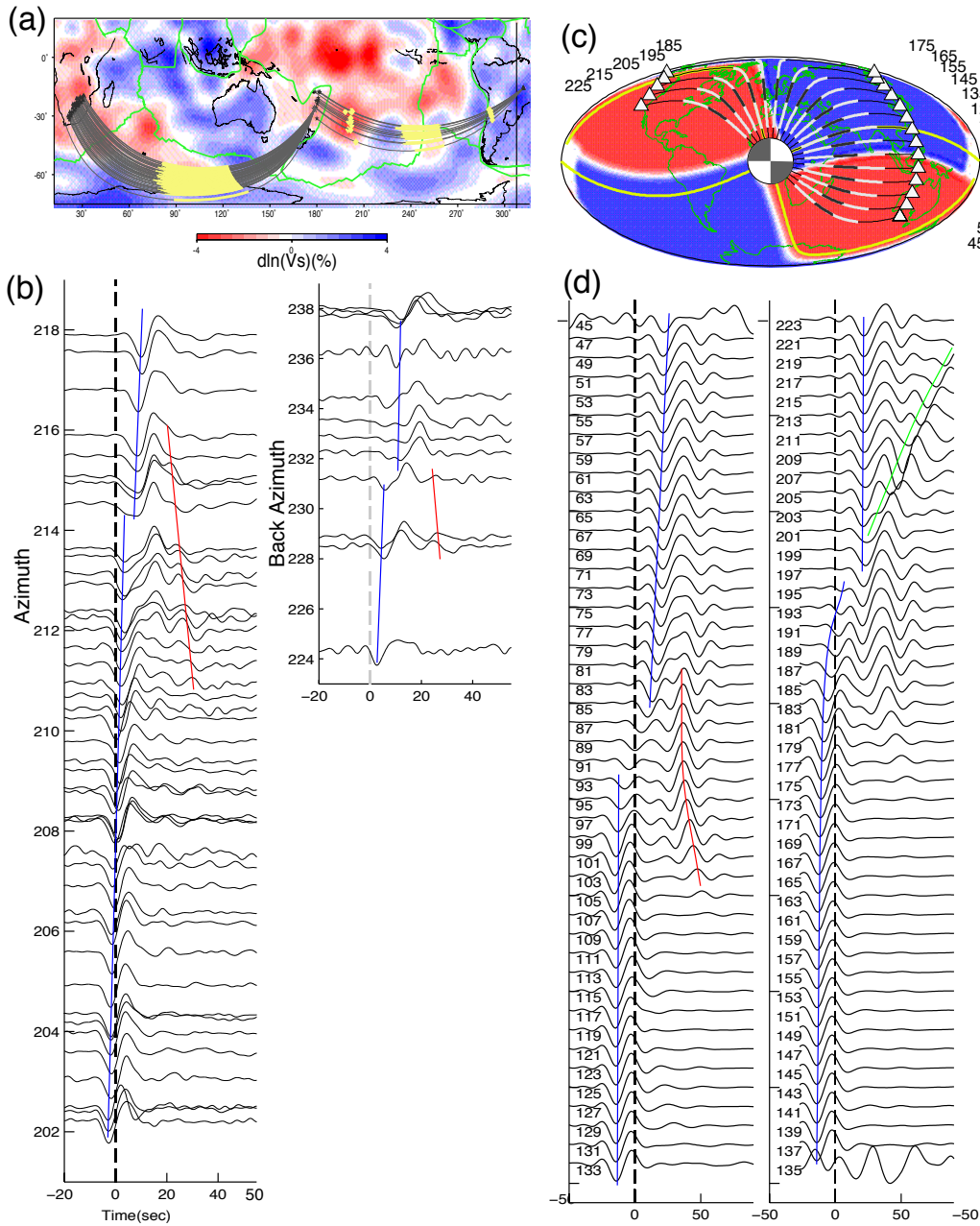


Figure 12.40: (a) Earthquakes (stars), stations (triangles), and projections of the raypaths. Background model is the shear velocity model SAW24b16 (*Mégnin and Romanowicz, 2000*) at the CMB. The thick yellow lines show the diffracting portion of the paths on the CMB. (b) Observed velocity waveforms. A bandpass filter with corner frequency at 0.01 to 0.125 (Hz) is applied. Left; Waveforms from the event 19970904 in Fiji-Tonga region recorded at South Africa. Right; Waveforms from 12 events in Fiji-Tonga region recorded at the station BDFB in Brazil. (c) The shear velocity model used in the CSEM synthetic waveform calculation. Each quadrant has either -3% or +3% constant anomaly with respect to PREM. (d) Synthetic waveforms calculated using CSEM for the model shown in (c). The numbers on the left side of each trace indicates the station number. Left; the source is located on the fast side of the interface. Right; the source is located on the slow side of the interface. The blue lines follow the trough of the first arrivals. When the source is located in the slow anomaly region (Right panel), large postcursors (green lines) are observed at the receivers located in the slow regions. They correspond to paths turning within the velocity gradient. They are observed at stations 221-203. When the source is located in the fast region (Left panel), a reflected wave is observed at the stations in the fast regions and refracted wave, which first enters the fast region and then enters the slow region by refraction, is observed at stations in slow regions. Both waves are shown by red lines. They are observed at stations 81-105.

22. Hemispherical Transition of Seismic Attenuation at the Top of the Earth’s Inner Core

Aimin Cao and Barbara Romanowicz

22.1 Introduction

The Earth’s inner core is formed by a freezing process of iron as the liquid outer core gradually cools (*Jacobs, 1953; Stacey, 1980*). Because the outer core material is not pure iron, some of the light elements are excluded from the inner core during this dynamic process, to power the geodynamo, while the residual is likely kept within a mushy layer at the top of the inner core (*Fearn et al., 1981*). Thus, constraining the characteristics of the mushy layer at the top of the inner core, as revealed by seismic velocity and attenuation measurements, should give us important insights into the dynamics of the Earth’s core.

The outer core Q_α is usually regarded as infinite ($\geq 10,000$) (*Cormier and Richards, 1976*), but the estimated Q_α in the inner core is constrained to be less than 450. This huge contrast indicates that a zone of decreasing Q_α with depth must exist beneath the ICB. However, this zone of decreasing Q_α should be confined to the top of the inner core, because multiple seismic observations confirm that Q_α increases with depth below a depth of approximately 100 km beneath the ICB (e.g., *Souriau and Roudil, 1995*). Therefore, the existence of a transition zone at the top of the inner core, where Q_α turns from decreasing to increasing with depth, seems likely.

In order to study the seismic structure at the top of the inner core, the most suitable body wave phases are PKIKP and PKiKP in the epicentral distance range from 120° to 144° (Figure 12.41). In this distance range, PKIKP samples the top 0-110 km of the inner core and PKiKP is reflected from ICB. The two phases have almost the same ray paths in the mantle and very close ray paths in the outer core. Hence the assumption that they experience almost the same heterogeneities in the mantle and outer core is valid in a first approximation. The differences in travel times and amplitudes can therefore be attributed to the vicinity of the ICB.

Unfortunately, these two phases present a great challenge. The separation of PKIKP and PKiKP is very small. For example, it is less than 1.3 seconds when the epicentral distance is less than 135° (when referred to the seismic reference model PREM (*Dziewonski and Anderson, 1981*)). On the other hand, the source time functions are usually longer than 3.0 seconds for events of $m_b \geq 5.5$ (*Cormier and Choy, 1986*). Interference between the two phases seems inevitable. We have developed a direct, but arguably effective, approach to circumvent the complex issue of event source time functions and directivities.

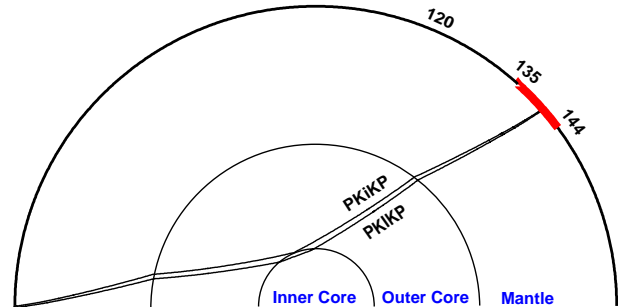


Figure 12.41: Ray paths of PKiKP (reflected P wave from the ICB) and PKIKP (P wave passing through the inner core). The two phases may appear simultaneously as early as 120° , but we can only obtain well-separated PKIKP and PKiKP phases in the epicentral distance range from 135° to 144° .

22.2 Data, Method, and Results

We systematically downloaded both broadband and short-period vertical component seismograms from IRIS DMC, GRF, GRSN, Jarray, and F-net seismic networks corresponding to recordings in the epicentral distance range of $134^\circ - 144^\circ$, for intermediate and deep earthquakes (focal depth >70 km, $M_w \geq 5.5$). These deeper events have shorter source time functions and higher signal-to-noise ratios than shallow events. To preprocess the seismograms, we employed a strictly narrow band-pass filter with corner frequencies of 0.7 and 2.0 Hz (corresponding to 1.5 and 0.5 seconds in period). The goal is to try to retrieve events whose 1.0 Hz energy was released in a short time and impulsively (within about 1.0 second), no matter how long their overall source time functions were. For this kind of events, we expect to observe pairs of well-separated PKIKP and PKiKP phases. In this paper, we directly measure amplitude ratios of PKIKP versus PKiKP in the time domain in order to estimate Q_α at the top of the inner core.

Our method requires to account for the phase shift of PKiKP with respect to PKIKP. Because PKiKP is a post-critically reflected wave at the ICB, the phase shift between PKiKP and PKIKP is approximately in the range of 142° to 163° (arguably close to 180°) in the epicentral distance range of our study. This means that if we reverse (that is multiplying the corresponding portion of the seismogram by -1) the PKiKP phase, the two phases should be very similar, as we verified using

synthetic seismograms.

After data preprocessing, our data-picking criteria are as follows: (1) the signal-to-noise ratio before the identified PKiKP is ~ 6 or more; (2) the signal-to-noise ratio within about one duration of the waveform after the identified PKiKP is ~ 3 or more; (3) the identified PKiKP and PKiKP phases are well-separated; (4) the reversed PKiKP waveform is similar to the PKiKP waveform. Following the above criteria, we successfully selected 280 pairs of high-quality PKiKP and PKiKP phases.

This large dataset of well-separated and similar PKiKP and reversed PKiKP waveforms provides us a unique opportunity to explore the seismic structure at the top of the inner core. In order to study the P-wave velocity structure, we first measure the differential travel time between PKiKP and PKiKP by means of cross-correlation, and then calculate the differential travel time residuals between PKiKP and PKiKP with respect to the reference seismic model PREM. In order to study the Q_α structure, we first measure the peak-to-peak amplitude ratios of PKiKP to PKiKP, and then estimate Q_α from these amplitude ratios after applying corrections for geometrical spreading, transmission, and reflection.

For differential travel time residuals, our results show a striking hemispherical pattern in the epicentral distance range 135° to 142° (corresponding to depths of approximately 32 to 85 km beneath the ICB) (Figure 12.42a), in agreement with the observations of *Niu and Wen* (2001) and *Garcia* (2002). Beyond 142° , the robust hemispherical pattern is not as clear.

For quality factor Q_α , our results also show a reliable hemispherical pattern almost in the same epicentral distance range (135° - 141.5°) (Figure 12.42b). In the western hemisphere Q_α decreases as a function of distance. In the eastern hemisphere, Q_α increases as a function of distance. Beyond an epicentral distance of 141.5° , the hemispherical pattern in Q_α disappears, as does that in the differential travel time residuals.

The P velocity and Q_α variations are compatible with an interpretation in terms of small hemispherical variations of temperature at the top of the inner core (*Sumita and Olson*, 1999) and their influence on the morphology of porosity and connectivity of liquid inclusions in the mushy zone. The disappearance of the differences in Q_α beneath 85 km provide constraints on the likely depth extent of the mushy zone.

22.3 Acknowledgements

We thank the following networks and data centers for providing the high quality data used in this study: IRIS-DMC, GRF, GRSN, J-array, and Fnet.

22.4 References

Cormier, F., Choy, G.L., A search for lateral heterogeneity in the inner core from differential travel times

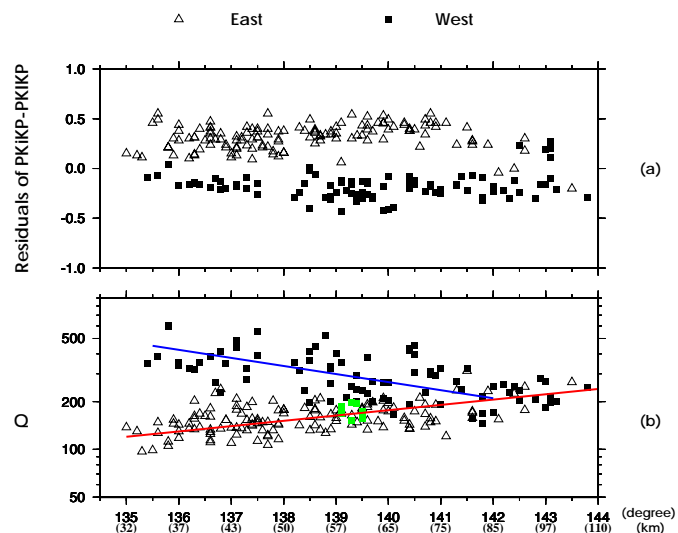


Figure 12.42: (a) Differential travel time residuals (referring to PREM). (b) Q_α with respect to the epicentral distance and depth beneath the ICB. High-lighted green squares show the data sampling offshore northwest of Africa. The event epicentral distances were all calibrated with a reference focal depth 100 km.

near PKP-D and PKP-C, *Geophys. Res. Lett.*, 13, 1553-1556, 1986.

Cormier, V.F., Richards, P.G., Comments on 'The damping of the core waves' by Antony Qammar and Alfredo Eisenberg, *J. geophys. Res.*, 981, 3066-3068, 1976.

Dziewonski, A.M., Anderson, D.L., Preliminary reference Earth model, *Phys. Earth Planet. Inter.*, 25, 297-356, 1981.

Fearn, D.R., Loper, D.E., Roberts, P.H., Structure of the Earth's inner core, *Nature*, 292, 232-233, 1981.

Jacobs, J.A., The earth's inner core, *Nature* 172, 297, 1953.

Garcia, R., Constraints on upper inner-core structure from waveform inversion of core phases, *Geophys. J. Int.*, 150, 651-664, 2002.

Niu, F., Wen, L., Hemispherical variations in seismic velocity at the top of the Earth's inner core, *Nature*, 410, 1081-1084, 2001.

Souriau, A., Roudil, P., Attenuation in the uppermost inner core from broad-band GEOSCOPE PKP data, *Geophys. J. Int.*, 123, 572-587, 1995.

Stacey, F.D., The cooling earth: A reappraisal, *Phys. Earth Planet. Inter.*, 22, 89-96, 1980.

Sumita, I., Olson, P., A laboratory model for convection in Earth's core driven by a thermally heterogeneous mantle, *Science*, 286, 1547-1549, 1999.

Chapter 13

Appendices

